NTNU – Trondheim
Norwegian University of
Science and Technology

Synthesis And Characterization Of Noble Metal Nanoparticle Impregnated Metal-Organic Frameworks

Karsten Granlund Kirste

Chemistry
Submission date: May 2013
Supervisor: Karina Mathisen, IKJ
Co-supervisor: Odd Reidar Gautun, IKJ

Norwegian University of Science and Technology
Department of Chemistry

Masterthesis

Synthesis and characterization of noble metal nanoparticle impregnated metal-organic frameworks

Karsten Granlund Kirste

NTNU
Det skapande universitetet

Acknowledgement

The work of this Master's thesis has been carried out at the Norwegian University of Science and Technology (NTNU), mainly at the Department of Chemistry and at the Swiss-Norwegian Beamline at the European Synchrotron Radiation Facility. NTNU is acknowledged for economically supporting the stay at ESRF.

I would like to thank my supervisor Karina Mathisen, for always having time and an open door for my questions and me. I have appreciated working under your guidance and all the moments with great humor and for you believing in me. My co-supervisor Odd Reidar Gautun deserves also attention for his interest in my work and for his patience with me when I was not into the organic chemistry way of thinking.

Tina Kristiansen, Katrine Bøyesen, Rajesh Raju and Stian Forselv deserves attention for their willingness and always being there and helping me when I had troubles in the lab or with data analysis. Julian Tolchard, Susana Villa Gonzales and Elin Harboe Albertsen is acknowledged for their help with XRD, UV and adsorption-desorption measurements. I would like to thank Eugenia Mariana Sandru for kindly providing me with gold nanoparticles for the encapsulation experiments. The research group deserves a thanks for the group meetings, excursions, sjoelbak, quizzes, the christmas parties and for making the research group a pleasant place to be.

Thanks to Helene, Torstein and Terese for helping me proofread the thesis. Thanks to the extended faddergruppe 3 for all the fun these five years. Kaja, Heidi and kosekontoret deserve a huge thanks for all the great moments and for keeping me sane and alive the last period of this thesis. I

would like to thank Trygve for being the ultimate travel partner to the ESRF. I hope we can continue to be NTNU SYNCHROTRON TEAM in the future. I would like to thank Ragni and Thomas for being my partners in crime and for all the good times we have had together and for all the fun we are going to have. You are the best! And last but not least I would like to thank my mother for her unconditional love and support during these five years. I could not have done this without you.

Karsten Granlund Kirste

Trondheim, May 2013

Sammendrag

Metall-Organiske rammeverk (MOF) er en ny materialklasse hvor materialen porøse og krystallinske. Materialene består av uorganiske koordinasjonsenter som er knyttet sammen med organiske molekyler. Materialen har den fordelen at den kombinerer uorganisk materialvitenskap med den lett manipulative organiske kjemien. Dette har ført til materialer som lett kan designes og tilpasses bruksområde. Noen ulemper med MOF er at de lett dekomponerer ved høye temperaturer. Det har vist seg vanskelig å finne industrielle bruksområder for disse materialene. I dag forskes det blant annet på MOF til gasslagring, separasjon og katalyse.

MOF er porøse og har høyt overflateareal noe som gjør materialene til aktuelle kandidater som hetrogene katalysatorer ved deponering av aktive nanopartikler på overflaten. Porene i materialet kan definere størrelsen på nanopartiklene som blir dannet og fungere som molekylsikt og innføre begrensinger på reaktant, intermediat og produkt dersom katalysen utføres i porene. Målet med denne oppgaven har vært å lage til nye mulige katalysatorer av det metall-organiske rammeverket UIO-66, med nanopartikler av gull eller palladium og karakterisering og testing av disse.

I denne oppgaven har deponeringen av gull blitt forsøkt med en impregnering/deponering, reduksjons deponering og innkapsling av gull nanopartikler. Palladium har også blitt deponert ved hjelp av en reduksjonsdeponering på UIO-66. Videre har materialene blitt karakterisert ved hjelp av røntgendiffraksjon, adsorpsjons desorpsjons målinger, induktivt koplet plasma massespektroskopi og røntgen absorpsjons spektroskopi både *in situ* og *ex situ*. Til slutt har palladium-UIO-66 blitt testet for aktivitet mot Sonogashira, Suzuki-Miyaura og Mizoroki-Heck reaksjonene som normalt utføres av organopalladium komplekser.

De viktigste funnene i denne oppgavene er at de ulike teknikkene for gull deponering på UIO-66 gir lave vektprosent av gull (0,39 % på det beste) på bæreren og at partikkelstørrelsen blir for stor til katalyse. Videre har Pd-UIO-66 utvist katalytisk aktivitet mot Sonogashira, Suzuki-Miyaura og Mizoroki-Heck reaksjonene, noe som ikke ha blitt utført før på dette systemet. Imidlertidig ble det oppdaget at katalysatorene hadde dekomponert etter opparbeiding.

Abstract

Metal-Organic frameworks (MOF) is a new class of materials that are porous and crystalline. The materials are made of inorganic coordination centers linked together by organic molecules. MOFs have the advantage of the combination of inorganic units connected with highly manipulative organic molecules. The result is materials that can be specifically designed for the area of application. The disadvantage of MOFs is the low thermal stability which leads to decomposition of the framework at higher temperatures. The industrial applications of MOFs are few, but research for the use of MOFs for gas storage, separation and catalysis is being done.

MOFs are porous and have high surface areas and this makes the MOFs interesting candidates as heterogenous catalysts with active nanoaparticles in the framework. The pores in the framework can define the size of the nanoparticles and also function as molecular sieves and thereby introduce catalytic selectivity on the reactant, intermediate and products if the catalytic process is carried out in the pores. The goal of this Master's thesis is to prepare new catalysts with gold or palladium nanoparticles deposited on the UIO-66 framework and the characterization and testing of these.

The metal-organic frameworks MOF-5 and UIO-66 have been synthesized. Gold was deposited onto the UIO-66 framework by impregnation deposition, reduction and encapsulation of pre-made gold nanoparticles. Palladium was deposited onto the UIO-66 framework by reduction deposition. The materials have been characterized by X-ray diffraction, adsorption–desorption experiments, inductively coupled plasma mass spectrometry and X-ray absorption spectroscopy both *in situ* and *ex situ*. The Pd-UIO-66 has been tested towards catalytic activity of the Sonogashira, Suzuki-

Miyaura and Mizoroki-Heck reactions normally performed by organopalladium complexes.

In this thesis the investigated methods for gold deposition gave low loading levels of gold (at best 0.39 wt%) on the framework and the particle sizes detected were too large for catalytic activity. The palladium loading levels were 2.34 wt% and 2.48 wt%. The Pd-UIO-66 showed catalytic activity for the Sonogashira, Suzuki-Miyaura and Mizoroki-Heck reactions, which has not been previously reported. However the catalyst was found to decompose after the work up.

Contents

List of symbols and abbreviations

$\Delta\mu_0(\mathbf{E})$	Energy difference at threshold energy E_0
θ	Bragg angle in X-ray diffraction
λ	Wavelength of X-rays
ρ	Density of material (in surface area measurements)
χ	Ratio of desorption rate constants for 1st & 2nd layer
α	Slope of curve, BET isotherm
η	Intersection point of curve, BET isotherm
λ	Inelastic mean free path of the electron
σ	Debye-Waller factor of the j^{th} shell
$\chi(\mathbf{E})$	EXAFS function
$\mu(\mathbf{E})$	X-ray absorption coefficient
$\phi(\mathbf{k})$	Phase alteration
$\hbar$	Reduced Planck constant
$\mu_0(\mathbf{E})$	Background of the atomic absorption
$\mathbf{2kR}_j$	Phase change for photoelectron
$\mathbf{A}_j(\mathbf{k})$	Amplitude function of j^{th} shell
AFAC	Amplitude reduction factor
Agglomerate	Primary particles rigidly joined together
Aggregate	Weak assembly of primary particles
BET	Brunauer Emmet Teller
CVD	Chemical vapor deposition
d	Lattice spacing in crystal
DMF	Dimethyl formamide
E	Energy
$\mathbf{e}^{\frac{-2r}{\lambda}}$	Exponential attenuation of the electron

$\mathbf{e}^{2k^2\sigma_j^2}$	Reduction term for disorder in the solid
$\mathbf{E}_0$	Threshold energy of the absorption
$\mathbf{E}_f$	Fermi energy
ESRF	European Synchrotron Radiation Facility
EtOAc	Ethyl acetate
EtOH	Ethanol
EXAFS	Extented X-ray absorption fine structure
$\mathbf{F}_j\mathbf{(k)}$	Element spesific backscattering factor for the jth shell
h k l	Miller indices in lattice
HDPXRD	High Definition Powder X-ray Diffraction
$\mathbf{I}_0$	Intensity of incident X-rays
$\mathbf{I}_f$	Fluorescent radiation
$\mathbf{I}_t$	Transmitted intensity
ICP-MS	Inductively Coupled Plasma Mass Spectrometry
j	The jth neighbor shell
k	Wavenumber
$\mathbf{K}_\alpha$	Copper X-ray irradiation energy
keV	Kilo electron volts
L	Characteristic length (in surface area measurements)
m	Mass of photoelectrons
macro	$>$ 50 nm pore size
MeOH	Methanol
meso	2-50 nm pore size
micro	$<$ 2 nm pore size
MIL-101	Type of MOF, named after the Material Institut Lavoisier
MIXMOF	Mixed metal-organic framework
MOF	Metal-organic framework
MOF-5	Type of MOF
$\mathbf{N}_j$	Coordination number of the jth shell
NIST	National Institute of Standards and Technology
NTNU	Norwegian University of Science and Technology
P	Pressure
$\mathbf{P}_0$	Equilibrium pressure
PCP	Porous coordination polymer
PXRD	Powder X-ray diffraction
$\mathbf{R}_j$	Distance between absorbing atom and the jth shell
$\mathbf{R}_{M-M}$	Interatomic distance in a metal
$\mathbf{R}_{Pt-Pt}$	Bonding distance in platinum

RT	Room temperature
S_0	Amplitude reduction factor
SBU	Secondary building unit
SCXRD	Single crystal X-ray diffraction
SNBL	Swiss- Norwegian Beam Line
sod-ZIF-8	Type of MOF, Zeolitic imidazolate framework
TEM	Transmission electron microscopy
UIO-66	Type of MOF, named after the University of Oslo
UV	Ultraviolet
V_0	Volume of gas adsorbed in one monolayer
V_a	Volume of adsorbed gas
x	Sample thickness, Lamberts law
XANES	X-ray absorption near edge spectroscopy
XAS	X-ray absorption spectroscopy
XRD	X-ray diffraction
ZIF-66	Type of MOF, Zeolitic imidazolate framework

List of Figures

List of Tables

Chapter 1

Theory

1.1 Metal Organic Frameworks

Metal-Organic frameworks — bridging the gap between organic bottom up design with inorganic materials to a whole new research field of functional/advanced materials. Metal-Organic Frameworks are 2D or 3D, porous, crystalline and robust networks and are a relative new class of materials.[1] Metal-Organic frameworks are often called porous coordination polymers. The materials consists of coordination centers connected by linkers. The coordination centers are cations or inorganic coordination complexes called SBU (Secondary building unit).[2,3] The linkers in metal-organic frameworks are organic molecules with electron donating functional groups. The most popular linking units are carboxylate compounds, imidazole compounds and pyridine compounds,[2,4–8] but there also exist more exotic linkers for more breathtaking materials with amazing properties[9,10] The names of the different MOFs are arbitrary. There is no existing nomenclature for naming the different materials, because the chemical formulas are long and complex and there are often several versions of the same MOF due to different degree of incorporation of solvent. Instead MOFs are often given common names of three letters and a number i.e: UIO-66, MOF-5, MIL-101 and ZIF-66. The three letters may refer to the "birthplace" of the MOF (UIO-66: University of Oslo, MIL-101: Matérial Institut Lavoisier[4,11]), the type (ZIF-66: Zeolitic im-

idazolate framework) or based on the properties of the material. MOFs that have topologies similar to a zeolite is often named with the short name of the zeolite topology in lower case letters before the original name (sod-ZIF-8[12]). Other MOFs with structures similar to other materials are denoted the same way. The three letter lowercase topology code is called a net, i.e pcu = primitive cubic, bcu = body centered cubic, dia = diamonoid. The assigning of a net and topology is a difficult procedure and there are several different notations.[13] If there is made similar MOFs with the same net, but with another linking unit, the new framework is usually named as an IRMOF (Iso-Reticular) and a respective number. For reticular chemistry there exists a resource web-page[14] similar to the zeolite resource page.[15] MOFs with different types of linkers are called MIXMOFs.

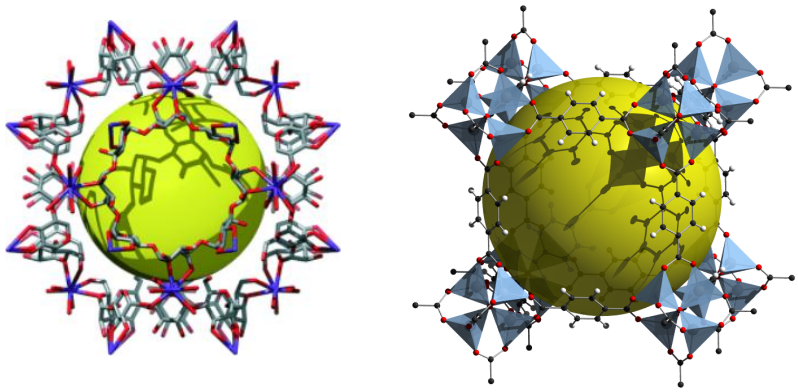

Figure 1.1: Different coordination centers in metal-organic frameworks. Left: A potassium ion as a coordination center with a 8 coordination (marked in violet). The yellow ball is illustrating the largest volume that can be occupied by a guest molecules. The sphere is 17 Å in diameter. Adopted from[9] Right: MOF-5 with its coordination center consisting of oxygen (red) and Zn^{2+} inside the tetrahedra. The yellow sphere is 18,5 Å in diameter.[16]

The synthesis of MOFs is a relatively simple procedure,[4,11,17] but the challenge of making MOFs is proper evacuation of the pores. The MOFs are usually synthesized in polar solvents to ensure that both linker and metal source is solubilized. The reaction mixtures are usually heated in a closed vessel (solvothermal and nonsolvothermal synthesis) or the precipitation of the MOF happens at room temperature (direct precipitation). The pH of

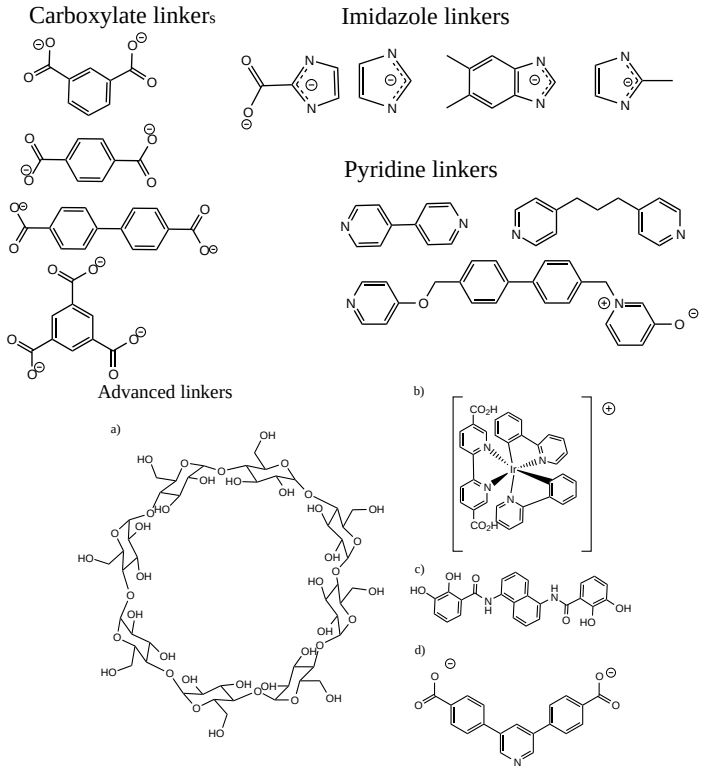

Figure 1.2: Linkers used in MOF-synthesis. The imidazole, carboxylates and pyridines are the most popular in MOF synthesis. The advanced linkers surges specific functions a) γ-cyclodextrine (edible and large), b) light harvesting linker c) and d) Polydendate and tridentate

the reaction mixtures are often adjusted to keep the linkers protonated or deprotonated. After the synthesis the MOF is washed with the same solvent as in the reaction mixture to wash away excess linker and byproducts formed during the synthesis. The solvent exchange process is the next step where the polar solvent is exchanged with a more volatile solvent. The MOF is then dried at reduced pressure or filtered and then dried at reduced pressure and elevated temperature.[8] Very often the pores collapse due to compression of the framework when the solvent is removed, which can be reduced by drying with supercritical CO_2. The measured surface area is usually reported to higher values when a supercritical fluid is used to dry the framework.[18] The linkers can be altered after the material has

precipitated by a post-synthetic modification to activate the material for an application.[19,20]

1.1.1 Properties and applications

MOFs show incredible properties. The most appreciated property of MOFs are the almost endless chemical versatility, since the linking units are organic molecules the synthesis and design of new linking units are almost unlimited. Compared to other porous materials the functionalization of pores can be quite difficult and a demanding process, but with MOFs the desired functionality can be incorporated in the linker or in the coordination center and included in the MOFs quite easily. The functionalization of linkers may result in catalytic active materials with embedded catalytic activity in the framework itself or[21,22] light absorption properties,[10,23,24] The list of possible properties is almost endless and only some properties are mentioned here. The MOFs also show incredibly high surface areas compared to other porous solid state materials. The current record for gas absorption properties is slightly above 7000 $\frac{m^2}{g}$.[18] An obvious application for MOFs is gas storage and separation because of large pores and large surface areas, but basically any application relating to adsorb compounds inside the pores is possible, i.e drug delivery.[25–27]

Table 1.1: Properties of MOFs compared to other porous materials. Adopted from Ranocchiari and van Bokhoven.[5]

Property	**Zeolites**	**MOFs**	**Mesoporous mat**
Crystalline	Yes	Yes	No
Homog. surf.	Yes	Yes	No
Surface area	$< 600\ m^2g^{-1}$	Up to $7000\ m^2g^{-1}$	$< 2000\ m^2g^{-1}$
Diffusivity	Low	Low to high	High
Thermal stability	High	Low to medium	Medium
Chemical stability	High	Variable	High
Chemical versatility	Low	High	Medium–low

The disadvantage of MOFs is the low thermal stability caused by the organic linkers making applications such as high temperature catalysis impossible since the MOFs decompose before the temperature for catalysis is reached. Often the synthesis of MOFs results in interpenetrating

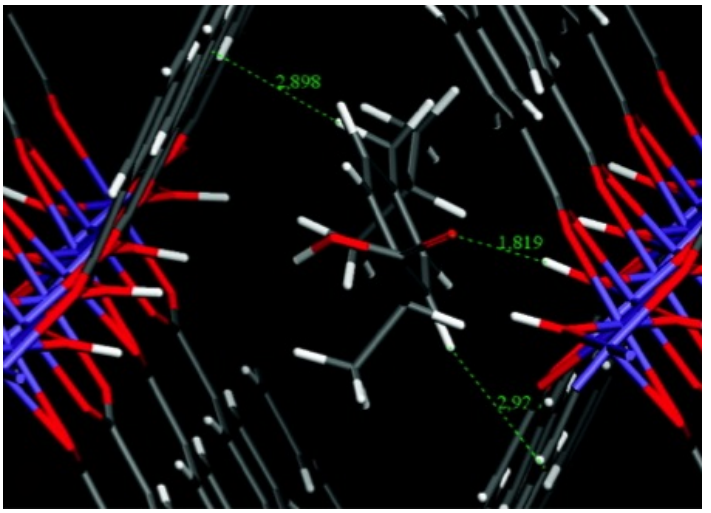

Figure 1.3: Ibuprofen modeled inside a MOF pore. Reprinted with permission from Horcajada.[26] Copyright ©2008 American Chemical Society

networks which is two MOF networks entangled inside each other, lowering the pore sizes and thereby excluding a bigger size range of guest molecules.[3,5,13]

1.1.2 MOF-5

MOF-5 was first synthesized by Yaghi *et al* , and is the archetype of metal-organic frameworks. The framework consists of coordination centers with 4 tetrahedrally coordinated zinc ions connected with corner sharing tetrahedra and the coordination centers are linked together by 1,4-benzenedicarboxylate linkers as seen in figure Figure 1.1.[16,28] The network formed is cubic and has a BET surface area of 3500 $\frac{m^2}{g}$.[29,30] The thermal decomposition point of MOF-5 is at 400 °C. MOF-5 is sensitive for humidity and decomposes after exposure to air.[31,32] The framework of MOF-5 has catalytic activity for Friedel-Craft alkylation.[33]

1.1.3 UIO-66

UIO-66 is a metal organic framework consisting of 1,4-benzene-dicarboxylate linkers connected to $Zr_6O_4(OH)_4$ octahedron. In the formed framework there are super tetrahedron cages and super octahedron cages as seen in Figure 1.4. The surface area of UIO-66 is measured to approximately 1100 $\frac{m^2}{g}$. UIO-66 is also one of the few MOFs with a remarkable stability of the structure and can withstand temperatures up to 375 °C and stable in DMF, water, acetone and ethanol. It is also reported that the framework can handle hydrochloric acid in small amounts. The framework is able to maintain some crystallinity upon exposure to sodium hydroxide. Upon heating the framework loses the hydroxilic group and forms ZrO_6 clusters. This is called the dehydroxylated version of UIO-66 and the consequence of this dehydroxylation is that the clusters contract.[4]

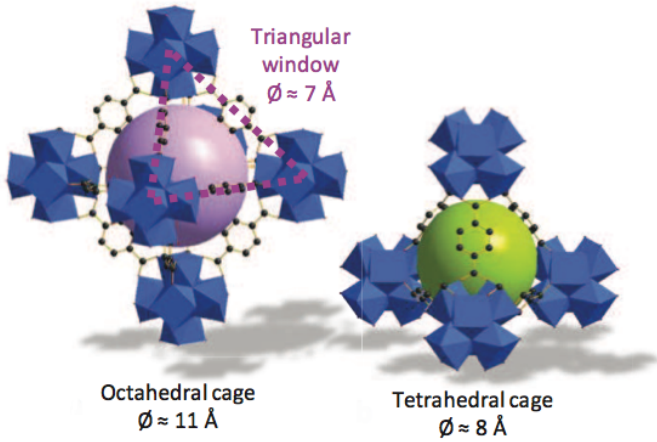

Figure 1.4: Right: The tetrahedron cage formed in UIO-66. Left: The octahedron cage formed in UIO-66. Adopted from Mendes *et.al*[34]

1.2 Nanoparticles

A nanoparticle is a particle with at least two or more dimensions in the range of 1-100 nm. Nanoparticles exhibit properties that do not exist in the bulk phase. This might be absorption of wavelengths, emittance of radiation, catalytic properties or magnetism. Nanoparticles have discrete energy levels and not continuous energy bands, which is due to the high surface to volume ratio of nanoparticles.

1.2.1 Gold

Bulk gold is known as an inert metal, and its applications include currency and decorative properties. Gold nanoparticles have been utilized to color glass red in medieval times but the discovery of gold nanoparticles was not before the 1850s. The synthesis of gold nanoparticles in different sizes is well described by Turkevich, Goia and Brust.[35–38] The synthesis of gold nanoparticles is often based on a simple gold precursor such as auric acid, $HAuCl_4$, and a reduction agent. Turkevich, Brust and Goia have shown that gold is easily reduced by using a wide range of reducing agents. They have also shown that gold colloids may be stabilized in solution by adsorbing surfactants and chelating agents on the surface and thereby stopping agglomeration.

Gold and nanoparticles of gold do not oxidize, while many other transition metals form oxide layers on nanoparticles.[39] Gold nanoparticles can absorb radiation and hence get colors, or absorb radiation in the IR range due to the surface plasmon resonances.[40] It is also shown that nanoparticles with the size of 5 nm and below are catalytically active. First for supported gold nanoparticles for CO oxidation,[41] then later for water gas shift reactions, epoxidation of propene and reduction of NO_x.[42] Gold has shown activity towards a Sonogashira coupling reaction.[43] It has also been proven as a valuable homogenous catalyst for the activation of the addition of nucleophiles to double and triple C–C bonds, by acting as a Lewis acid.

In heterogenous catalysis, gold nanoparticles are usually supported on porous materials by CVD (Chemical vapor deposition) techniques[44] or precipitation / impregnation and followed by reduction on the surface

forming the nanoparticles.[45] Gold nanoparticles have also been made with diffusion of the gold precursor into the framework[46] or by encapsulation of already made gold particles.[47] The most common precursor auric acid also provides chloride ions which is a known catalyst poison and promotes sintering of particles.[48] Other gold precursors may be auric tetraamine nitrate or organo gold complexes. Supporting the gold nanoparticles prevents sintering and some supports promote catalysis by stabilizing active gold species. This is observed in MnO_2, CeO_2 and Fe_2O_3. In gold nanoparticles it is the atoms with lowest coordination that have electronic states corresponding to Au^+ and Au^{3+} which are catalytically active.[49] Gold particles supported on MIL-53 framework have shown activity towards the oxidation of alcohols, the mean particle size measured by TEM is 2.35 nm and has shown high conversion and selectivity.[50]

1.2.2 Palladium

Palladium is well know for its catalytic properties in homogenous catalysis in various organic coupling reactions.[51] In heterogenous catalysis palladium is know for its role as an oxidation catalyst in the three way catalytic converter.[52] There is not consensus on whether Pd catalysis happens on the nanoparticles or on smaller fragments released from the nanoparticles out into solution.[49,53]Nanoparticles of palladium have shown activity for, among other Heck reaction,[53] arylation of indoles,[54] Suzuki-Miyaura cross-coupling,[55] Sonogashira coupling[56] and hydrogenation.[57] Bimetallic nanoparticles of gold and palladium supported on an ethylene diamine grafted MIL-101 framework has shown synergism in hydrogen generation from formic acid..[58] The sizes of the nanoparticles of palladium in different reactions varies between 2.6-6 nm.[54–56] The size of the nanoparticles are measured with transmission electron microscopy (TEM). The preparation of palladium nanoparticles is similar to the methods used for gold. Stronger reducing agents are used for palladium.

1.3 X-ray Diffraction (XRD)

X-ray diffraction is a technique using monochromatic X-rays and is applicable to samples with long range order. When the X-rays are aimed at the material the long range ordering of the material will diffract the beam according to equation 1.1. The diffracted beam will, due to constructive interference, create maximums which may be detected. The constructive interference arises when the path length of the X-rays between the reflective planes is equal as illustrated in figure Figure 1.5.[2,59,60]

$$2d\sin\theta = n\lambda \tag{1.1}$$

d is the distance between two layers of diffracting atoms as illustrated in figure Figure 1.5, θ is the incident angle of the X-ray beam, n is an integer and λ is the wavelength of the X-rays.

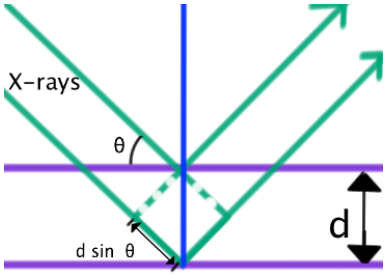

Figure 1.5: The principle of X-ray diffraction. Constructive interference is achieved when the path length ($2d\sin\theta$) between to planes in the compound is equal to an integer multiplied by λ

XRD may be performed on single crystals and the technique is named single crystal XRD (SCXRD). When the X-ray beam is directed at a single crystal the diffraction pattern which arises will consist of points. SCXRD is very useful for finding atomic positions, lattice type and crystal systems, but it requires long time scans to reduce signal to noise and the procedures are time consuming. SCXRD is not applied in this Master's thesis and will not be explained further. The sample may also be a powder consisting of random oriented crystallites in a size range. This technique is called powder X-ray diffraction (PXRD). When an X-ray beam is directed at a powder, each crystal will diffract the beam as in SCXRD. Instead of points

there are observed cones or circles and the reason for this is that since each crystal in the powder diffracts the beam and because of the random orientation, the direction of the points are random and will become circles or cones as illustrated in Figure 1.6.[2]

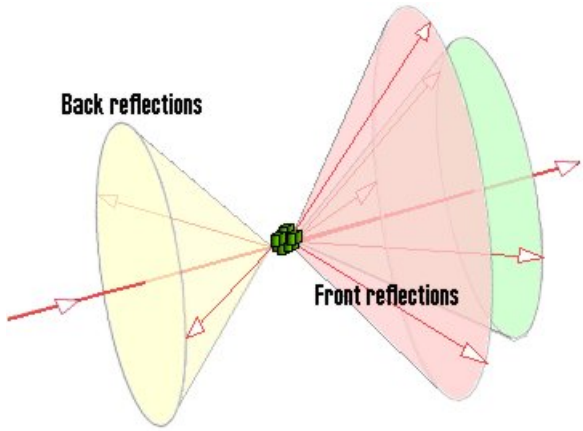

Figure 1.6: In PXRD the X-ray beam is diffracted into cones because of the random oriented crystallites. [61]

The diffraction pattern is recorded with respect to the angle of the detector compared to the incident beam. If a line detector (1D detector) is used, the detector moves in a line from 0°to the desired end of the scan (material dependent, but typically between 60-80°) as in Figure 1.7. This will result in a diffractogram which relates angle and intensity to the diffracted beam. A peak in the diffractogram is usually called a reflection. A 2D detector can be applied instead of the 1D detector and record the respective circles or half circles, which may reveal preferred orientation of the crystallites that causes incomplete circles and loss of peaks in the diffractogram. The 2D detectors are also usually faster than the 1D detectors but have poorer resolution than the 1D detectors.

The position of the reflection varies with the size of the unit cell of the material and the intensity of the peak is dependent of the number of electrons in the reflecting atoms/ions. If there are a lot of electrons in an atom or an ion the intensity of the peak is large and the position will also be at lower angles due to the increasing distance between reflective planes in the material. PXRD is very useful in detecting different crystallographic

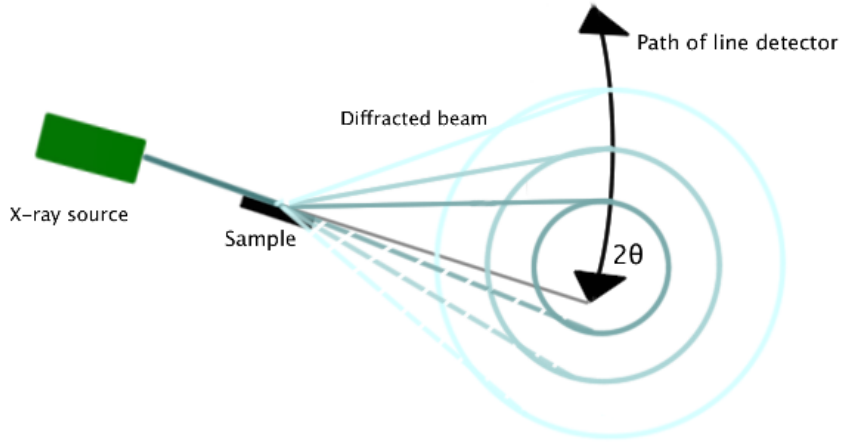

Figure 1.7: A schematic setup for a XRD diffractions experiments. The dotted lines illustrates the diffraction cones that are lost in the sample stand.

phases in a sample. In samples with multiple phases the corresponding diffractogram will consist of the diffraction peaks for all of the different phases, because the different phases will have different lattice types, crystal systems and thereby different cell parameters. The atomic positions, cell parameters, lattice types, composition and information about the crystal system of the sample may be extracted from a diffractogram by fitting the intensity of the experimental reflections to calculated diffraction patterns (Rietveld analysis) and absence or presence of reflections (lattice types).[2,59] There are a lot of databases offering diffraction data of already studied materials and enabling XRD as a fast and easy fingerprint technique by matching peaks with literature data.[62,63]Although XRD is a powerful tool for structure determination there are some limitations to the technique. The structure resolving is mainly done with single-crystal diffraction and PXRD is used for phase identification as much 3D information is lost when using a 1D detector. The low intensity and the wavelength of the X-rays produced on a laboratory scale will affect the obtained diffractograms by excluding small crystallographic features in the sample (i.e nanoparticles). Synchrotron radiation for diffraction experiments permits rapid data collection (due to increased intensity and brilliance) and higher resolution.[2,59,60]

1.4 Synchrotron light.[64,65]

A synchrotron is a particle accelerator and produces white radiation, which is a beam with a continuum of wavelengths. The synchrotron itself consists of a linear accelerator, a booster synchrotron, storage ring and beam lines.

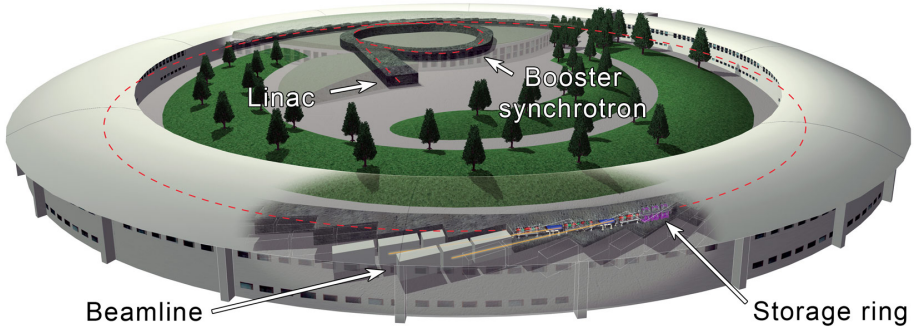

Figure 1.8: The different parts of the synchrotron at ESRF, Grenoble, France. Linac is the linear accelerator.[64]

The electrons are first accelerated with the linear accelerator and further accelerated with the booster synchrotron before injected in the storage ring where the production of the white beam to the beam lines takes place. The electron's velocity is almost at the speed of light. The electrons move in evacuated pipes in straight lines. White beam is made when the electrons are bent to follow the path of the storage ring which is done by a bending magnet. The bending magnet produces a strong magnetic field and then the electron is bent off and electromagnetic radiation is released tangentially to the bending. The bending magnet produces a spray of unfocused electromagnetic waves including X-rays. Synchrotrons may have insertion devices placed in between the bending magnets in straight distances. The insertion devices consist of many magnets with alternating polarities. When the electrons pass the insertion device the alternating magnetic fields of the different magnets makes the electrons undulate (oscillate/ wiggle) and thereby produce electromagnetic radiation along the electron path.

The produced white line is then directed through several mirrors and win-

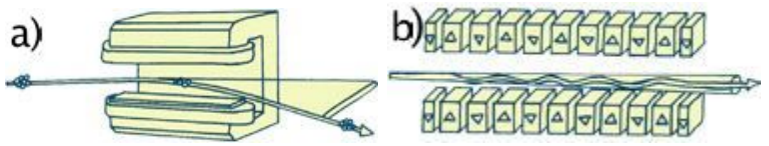

Figure 1.9: a) A bending magnet bending the trajectory of an electron. b) An insertion device wiggling an electron.[64]

dows filtering out uninteresting wavelengths. The mirrors also focus the beam. Then the beam passes the monochromator which selects electromagnetic radiation with only one energy. The now obtained X-ray beam is then directed into an experimental hutch where the X-ray passes through (in transmission mode) the reference detector, sample, and to the detector which detects the absorption of the sample. The benefits of synchrotron radiation is high flux which means high intensity photon beam that result in rapid experiments or the use of weakly scattering crystals, broad tunable spectrum with energies from microwaves to high energy X-rays and high brilliance ($\frac{photons/s}{(mrad)^2(mm\text{source area})^2(0.1\%\text{band witch})}$) allowing a highly collimated beam and spatial distribution of the beam.

1.5 Surface area measurements

Microporous and mesoporous materials tend to have high surface areas because of the extended pore systems which exist in the material. Metal-organic frameworks do also show high surface areas. For particulates the surface area may be defined as:

$$\text{Surface area} = \frac{\text{shape factor}}{\rho L} \tag{1.2}$$

Where L is the characteristic length, ρ is the density of the material and the shape factor is dependent of the shape of the particulate. Usually there exists different particle shapes and sizes. Aggregates and agglomerates will also exist and create interparticle pores which will cause a loss of surface. The surface area is also characterized as either external or internal. The internal surface area is defined as the area within the pore system as for zeolites, zeotypes and metal-organic frameworks, and it is also necessary

to define the internal surface area as the walls of all cracks, pores and cavities due to imperfections in the framework. The external surface is the surface area which is not within the pore system on the outer surface of the primary particles.[66]

The measurement of surface area is in concept a simple idea. The surface is measured with a gas that is adsorbed on the surface, and the amount of gas is measured when a monolayer is complete. The area of one molecule is then used to calculate the specific surface area. Depending on the gas used the different properties is measured. If H_2 or CO is utilized, the surface area of the active surfaces are measured since H_2 and CO adsorbed strongly and by forming covalent bonds to the surface (chemisorption). When the surface area of the active particles and the inert framework is measured, N_2 is the adsorptive. N_2 is used because it adsorbes with van der Waal forces (physisorption) and therefore adsorbs to all surfaces, not just the active surfaces as for H_2 and CO.Physisorption is reversible and chemisorption is not reversible.

The different pore sizes (In diameter: macro $>$ 50 nm , meso 2-50 nm, micro $<$ 2 nm) and the composition of the surface is the origin for the different adsorption isotherms classified by IUPAC,[67] the isotherms shown in figure Figure 1.10. Isotherm type *I* is characteristic for microporous adsorbents with monolayer adsorption and small external surfaces. Type *II* adsorption isotherm is characteristic for macro-porous and non-porous adsorbents with strong adsorbent interactions, typically where the material has the possibility to form several multilayers. Type *III* adsorption isotherm illustrates also adsorption in a macro-porous or non-porous material with weak interaction between adsorbent and adsorbate. Type *IV* is the adsorption isotherm for mesoporous materials with capillary condensation in the mesopores. The capillary condensation is illustrated with a hysteresis loop due to the condensed gas in the pores which will show a different vapor pressure (i .e kelvin equation). Type *V* is related to adsorption on a mesoporous material with weak interactions between adsorbent and adsorbate. Type *VI* shows stepwise adsorption in multilayers on a uniform and nonporous surface.[67–69]

The Brunauer Emmet Teller isotherm is used to calculate the specific surface area solids, and is used as a reference method. The Isotherm is based on the assumptions:

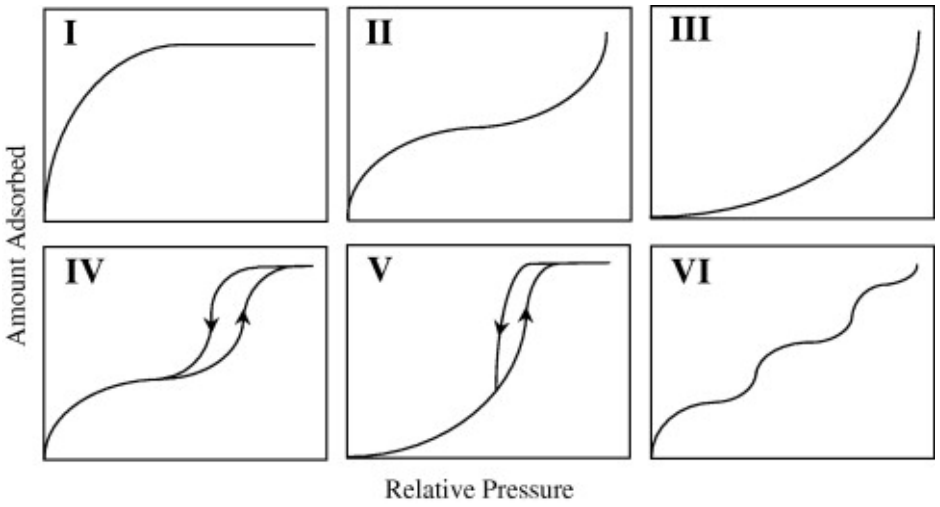

Figure 1.10: The IUPAC classification of adsorption isotherms

1. No lateral interactions between adsorbates.
2. All adsorption positions are equal in the first monolayer.
3. The adsorptive can adsorb on the first monolayer which acts as a new adsorption surface.
4. The heat of adsorption for the layers formed after the first is equal.

$$\frac{P}{V_a(P_0 - P)} = \frac{1}{\chi V_0} + \frac{(\chi - 1)}{\chi V_0}\frac{P}{P_0} \equiv \eta + \alpha\frac{P}{P_0} \tag{1.3}$$

Where P is the pressure, P_0 is the equilibrium pressure of the condensed gas on the surface, V_0 is the volume of gas adsorbed in one monolayer, V_a is the volume of adsorbed gas, χ is the ratio of desorption rate constants for the second and first layer of gas, $\eta = \frac{1}{\chi V_0}$ and $\alpha = \frac{(\chi-1)}{\chi V_0}$.[52]

The BET isotherm can be applied to nonporous, macroporous and larger mesoporous materials. For materials with smaller mesopores and micropores the capillary condensation causes error in the measurements. The solution to this problem is that the relative pressure ($\frac{p}{p_0}$) is measured in the range of 0,05-0,35 and then the surface area is interpolated.[69]

For MOF-5 the reported value of surface area varies between 700-3700 $\frac{m^2}{g}$[30] and a type V adsorption isotherm with no hysteresis.[28] UIO-66 is also reported as a type I adsorption isotherm with no hysteria and a surface area of approximately 1100.[4,70]

1.6 X-ray Absorption Spectroscopy (XAS)

X-ray absorption spectroscopy is the spectroscopic study of matter when X-rays are absorbed. The energies related to X-ray absorption spectroscopy are above the binding energies of core electrons to the absorbing element.[71] Elements absorb X-rays according to Lambert's law:

$$I_t = I_0 e^{-\ \mu(E)x} \tag{1.4}$$

where I_t is the transmitted intensity of the X-rays and I_0 is the intensity of the incident X-rays, $\mu(E)$ is the linear transmission coefficient which give the probability of X-ray absorption and x is the sample thickness.[72] μ is dependent of the sample density ρ, atomic mass A, X-ray energy, E, and the atomic number Z:

$$\mu \approx \frac{\rho Z^4}{AE^3} \tag{1.5}$$

Sharp increases in the X-ray absorption coefficient are so called absorption edges as seen in Figure 1.12. The position of the sharp rise in energy is often called the E_0 and is the threshold energy for the absorption. The sharp increase in the absorption coefficient corresponds to the ionization of core electrons from the element. This occurs because the incident X-rays have the same energy as the binding energy of the core electrons. This effect is called the photoelectric effect and the emitted electron is called a photoelectron (see Figure 1.11).[71,73]

As mentioned, the X-ray absorption coefficient is dependent on several factors including atomic number and weight as in equation 1.5. This makes XAS an element specific technique as the atomic number will influence the bond strength of the core electrons to the core. Typically XAS measurements are carried out at the K or L edge for the heavier elements with

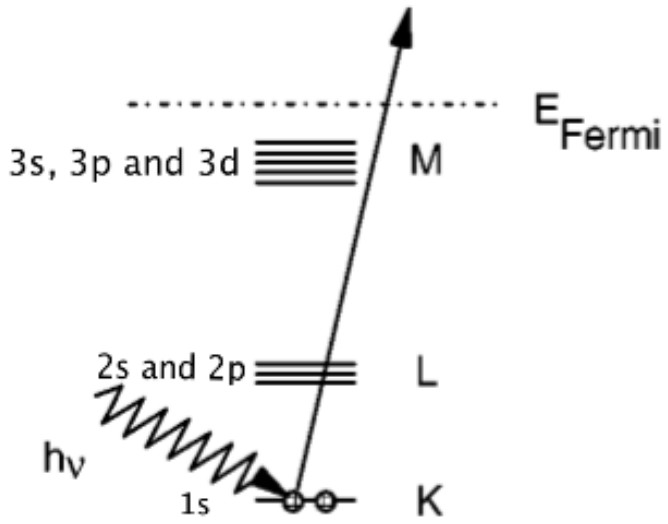

Figure 1.11: The photoelectric effect with an ionization of a core electron to continuum and this gives the sharp rise in the X-ray absorption measurements. Note that K, L and M corresponds to electrons with different principle quantum number. Adopted from Koningsberger.[72]

hard X-rays (< 2 keV).[71,72] The values of the various elements may be found at NISTs website. XAS for gold is usually recorded at the L_3-edge at 11919 eV.[74]

When an electron is ejected from an atom it leaves a core hole. This is regarded as an excited state. There are two main mechanisms for describing the relaxation process of the core holes. The first mechanism is fluorescence decay, in which electrons higher in energy fills the vacancy of the ionized electrons, and emits fluorescence radiation to lower the energy. The other main relaxation process is by Auger decay. Auger decay is when an electron higher in energy than the core hole is relaxed to the core hole in energy. As a consequence of the relaxation there exists excess energy in the atom and another electron closer to the fermi energy gets emitted. Typically fluorescence dominates as the relaxation process of the excited atoms/ions in the hard X-ray mode. XAS may be recorded in transmission mode according to equation 1.6 or in fluorescence mode according to

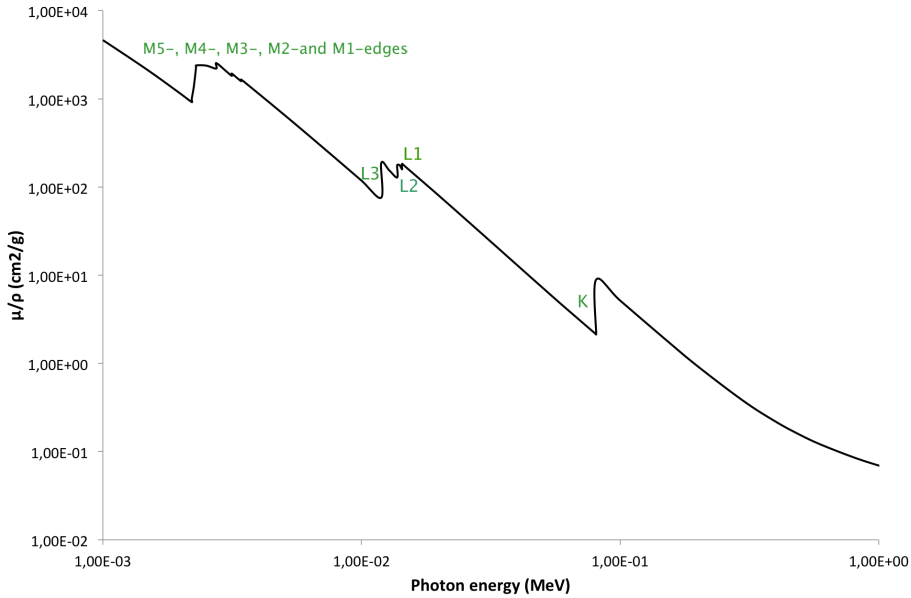

Figure 1.12: The behavior of $\frac{\mu}{\rho}$ (X-ray absorption coefficient) for Au (Z=79) from equation 1.5. The different absorption edges are indicated.[75]

equation 1.7.[71]

$$\mu(E) = \log \frac{I}{I_0} \tag{1.6}$$

$$\mu(E) \propto \frac{I_f}{I_0} \tag{1.7}$$

XAS spectra are divided into two main areas depending on how the ionization process is proceeding at the absorbing atom: X-ray Absorption Near edge Spectroscopy (XANES) and Extended X-ray Absorption Fine Structure (EXAFS). XANES is focusing on the features of the absorption spectra slightly before the absorption edge and 50 eV after the absorption edge, while EXAFS are based on observation of the fine structure from 50 eV and approximately 600-1000 eV after the absorption edge as seen in Figure 1.13.

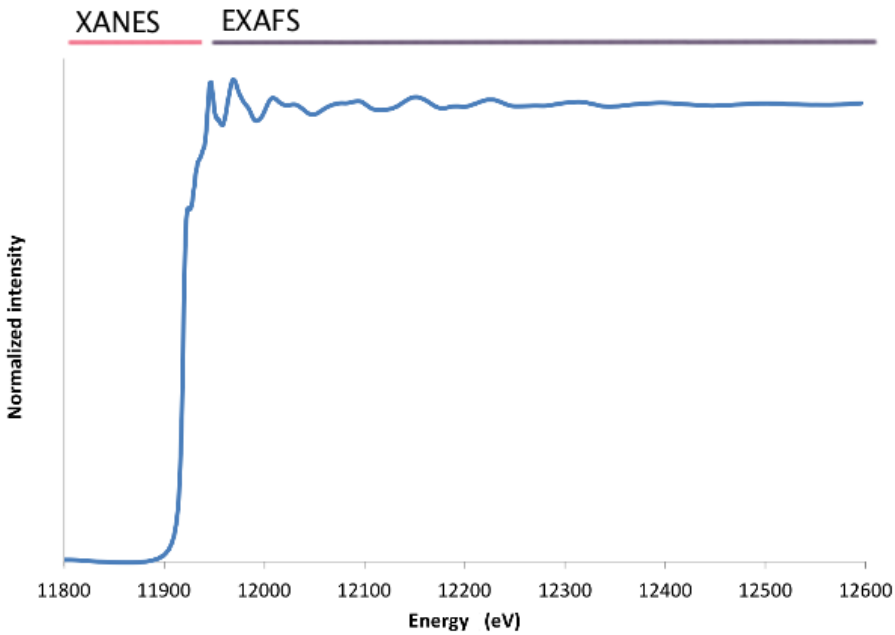

Figure 1.13: The regions used for XANES and EXAFS, here for a gold sample

1.6.1 X-ray Absorption Near Edge Structure (XANES)

The XANES range in energy is approximately 50 eV before the absorption edge (pre-edge), the absorption edge and approximately 30 eV after the absorption edge (post-edge) before the threshold energy for scattering is reached. There are quantitative theories for XANES but they are far more complicated than for EXAFS. Interpretation of XANES is mostly done in a qualitative matter. Nonetheless XANES may give quite a lot of valuable information as long as there exists XANES spectra of good model compounds. In the XANES range, the excitation of electrons is not energy rich enough to ionize the electrons to continuum but to other unoccupied electronic states close to the fermi energy. Therefore features in XANES spectra will highly reflect the electronic state of the absorbing atom/ion. Everything which affects the electronic state of the absorbing atom will therefore affect the XANES spectrum. This may be the chemical environment (types of neighbors, tetrahedral/octahedral coordination)

and oxidation state. XANES is therefore a fingerprint method.[60,71]

The pre-edge range may have absorption peaks which arise to transitions between energy states in the atom. These transition are governed by selection rules such as the Laporte selection rule and multiplicity. Pre-edge features (or the lack of) reveal information about the coordination geometry (tetrahedral vs octahedral) of the absorbing atom. The intensity of the pre-edge feature also gives insight into oxidation state and the degree of filling of orbitals. Since an empty orbital will have a higher possibility for receiving excited electrons.[59] Gold does not have pre-edge features in the metallic state. The cationic square planar coordination complex $Au(NH_3)_4$ does not show any pre edge features and is governed by the Laporte selection rule for kentrosymmetric molecules.

The position in energy for the absorption edge will also indicate the oxidation state as the higher the oxidation state on the absorbing atom the more difficult it is to remove electrons from the core because of the higher effective nuclear charge on the core electrons. To remove a core electron from a cation with a high oxidation state demands more energy and this will be observed in the XANES spectrum with the change in position of the absorption edge and the E_0. Gold is reported to have an E_0 of 11919 eV[76]

A white line is an intense absorption feature in the XANES spectrum as white lines overshoots the 0-1 normalization range. The name white line comes from the period when photographic plates were used to collect spectra and the white lines appeared on the photographic negative.[60] At the L_{III} edge Au^{3+} shows a prominent white line and this originates from excitations of the 2p orbital to 5d orbitals. This is because of Au^{3+} electronic configuration of $[Xe]4f^{14}5d^8$ compared to the metallic state where the electronic configuration is $[Xe]4f^{14}5d^{10}6s^1$, and excitations to the empty vacancy in the 5d orbital is possible for Au^{3+} and not for Au^0. In practice this statement must be modified because the 6s orbitals and the 5d orbitals are so close in energy and might hybridize making the white line transition possible and observable.[77]

1.6.2 Extended X-ray Absorption Fine Structure (EXAFS)

The fine structure in the extended X-ray absorption specters was recognized in the 1920s, but it was Lytle, Stern and Sayers in 1970 along with the development of synchrotrons with tunable X-rays who developed the structure determination theory of EXAFS.[78–80] The extended X-ray absorption fine structure stretches approximately 30 eV from the absorption edge and ends approximately 900 eV from the absorption edge. When X-rays above the absorption edge hits the atom the ejected electron, in Figure 1.11, will be emitted from the absorbing atom as a wave. The electron wave can be seen as a spherical wave, which scatters off the neighboring atoms. The backscattered electron wave will travel back to the absorber. The two different waves will then create a fine structure, seen as oscillations in the XAS spectra, because of the interference created between the two waves as in Figure 1.14. The EXAFS area in an absorption spectra will therefore contain information about coordination number of the absorbing atom, distance between emitter and scatter, type of backscattering atom and the disorder in the bonding lengths.[71]

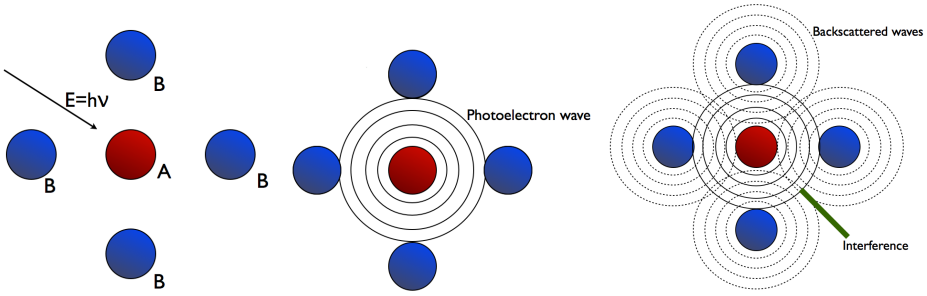

Figure 1.14: Above the absorption edge of an element the absorbed X-ray will cause an spherical electron wave to be emitted. The emitted photoelectron will be scattered back from the neighboring atoms and cause interference to occur for the central atom reabsorbing the wave. This will cause oscillations in the EXAFS area of the absorption curve.

The fine structure oscillations of the XAS spectra contain the desired information and it can be extracted as the EXAFS function $\chi(E)$. The EXAFS function is subtracted for atomic absorption and normalized with the absorption jump value to eliminate sample density:[81]

$$\chi(E) = \frac{\mu(E) - \mu_0(E)}{\Delta\mu_0(E)} \tag{1.8}$$

The X-ray absorption coefficient is μE, the background of the atomic absorption is represented by $\mu_0(E)$ and $\Delta\mu_0(E)$ is the jump in energy in the absorption at the threshold energy E_0. The functions are indicated in Figure 1.15. Equation 1.8 uses the energy as a variable, but as the nature of the photoelectron is considered as a wave, the conversion of the energy to the wavenumber k is necessary. This can be done using equation 1.9 where m is the mass of the photoelectron and $\hbar$ is the reduced Planck constant.[71,72]

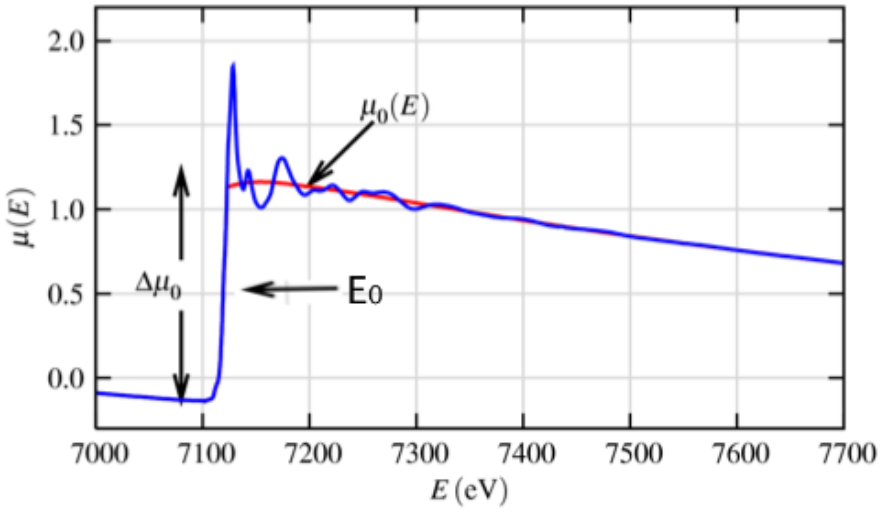

Figure 1.15: The XAS for FeO with the absorption jump $\Delta\mu_0$, the background function of atomic absorption and the threshold energy E_0 indicated. Adopted and modified from Newville.[71]

$$k = \sqrt{\frac{2m(E - E_0)}{\hbar^2}} \tag{1.9}$$

The presented equation 1.8 is a description of the experimentally achieved results. A more theoretically developed description of the EXAFS signal

or curve is desirable. The EXAFS equation presented here is an approximation based on being purely only single scattering. Single scattering means that the scattering path is directly between emitter thereafter to the backscatter and back again to the emitter as illustrated in Figure 1.14. The single scatter approximation is usually applied to heterogenous catalysts because the catalysts usually have high structural heterogeneity of the absorbing species and the first coordination shell is usually the main contributor for the signal.[81] There is also an approximation for the emitted wave and that is the plane wave approximation. The photoelectron wave is considered a plane wave where it assumes that the atomic radii are much smaller than the interatomic distances, and it is only valid for higher k-values ($k > 3\text{Å}^{-1}$),[72] and for high energy data the equation will be sufficient.[73] The theoretical EXAFS equation will then be:

$$\chi(k) = \sum_{j=1}^{Shells} A_j(k) \sin\left[2kR_j - \phi_j(k)\right] \tag{1.10}$$

j**:** the j^{th} neighbor shell
$A_j(k)$**:** The amplitude function of the j^{th} coordination shell.
$2kR_j$**:** The phase change associated with of the photoelectron from absorber to scatterer.
$\phi(k)$**:** The phase alteration due to electrostatic attractions from the nuclei.

The phase term describes how the electron wave travels to the scatter and back to the emitter in the term $2kR_j$, in addition there is the $\phi_j(k)$ which describes the phase change due to electrostatic interactions between the electron wave and the nuclei of the emitter and backscatters. The photoelectron wave experiences the central atom phase shift on the way from the absorber and on the way back from the scattering atom and the phase shift of the neighboring atom is only experienced on the way back from the scattering atom and this is reflected in the $\phi_j(k)$ function. The $\phi_j(k)$ is also dependent of the type of atom.[73,82]The amplitude term can be expanded into:

$$A_j(k) = \frac{N_j}{kR_j^2} S_0^2 F_j(k) e^{-2k^2\sigma_j^2} e^{\frac{2R_j}{\lambda(k)}} \tag{1.11}$$

R_j**:** The distance between the absorbing atom and the j^{th} shell

N_j**:** The coordination number of the j^{th} shell
S_0**:** The amplitude reduction factor. Corrections of relaxation effects in the emitting atom
$F_j(k)$**:** The element specific backscattering factor of the j^{th} shell.
λ**:** The inelastic mean free path of the electron
σ**:** The Debye-Waller factor of the j^{th} shell
$e^{\frac{-2r}{\lambda}}$**:** exponential attenuation of the electron.
$e^{-2k^2\sigma_j^2}$**:** The reduction term for static and dynamic disorder in the solid.

Equation 1.11 inserted into equation 1.10 yields "THE EXAFS" equation 1.12

$$\chi(k) = \sum_{j=1}^{Shells} \frac{N_j}{kR_j^2} S_0^2 F_j(k) e^{-2k^2\sigma_j^2} e^{\frac{2R_j}{\lambda(k)}} \sin\left[2kR_j - \phi_j(k)\right] \tag{1.12}$$

To extract accurate distances and coordination numbers it is necessary to Fourier transform the EXAFS equation as it is the sum of several oscillations. A critical point in EXAFS analysis is having accurate values of the backscattering factor and the phase alteration. Before, this was obtained by measuring experimental standards with known bond lengths and crystal structures. Today this is calculated by software prior to the analysis or tabulated from earlier calculations.[82] The oscillating curve obtained from the EXAFS equation decays rapidly. The amplitude of the oscillations decreases with the square of the distance between the emitter and backscatter and because of this dampening it is common to multiply the $\chi(k)$ with a power of k usually k raised to the second or third power.[71]

1.6.3 Limitations of XAS

XAS is a technique which may give a lot of valuable information, but it is important to know about the limitations for XAS to get reliable results. The absorption and fine structures detected is an average of the different species, and sizes. In order to get good results it is important that the size distribution of nanoparticles is narrow and not bimodal. In other words, homogenous samples is desired. EXAFS is also described as a local probe technique, meaning that the EXAFS equation rapidly

decays because of the mean free path $\lambda(k)$ term and the $\frac{1}{R^2}$ term. A description of the structure longer than 5 Å from the absorbing atom is meaningless. The resolution of EXAFS depends on the data range in k-space and coordination shells with almost similar distances will be hard to separate. Elements with almost similar atomic weight are hard to identify as much of the scattering properties are dependent of the atomic number (Z). Practically elements with low energy absorption edges may be difficult to probe because the X-ray beam will be absorbed by air and vacuum tube windows that the beam travels through from the bending magnet to the sample.[71,73,78,82]

1.6.4 Nanoparticles and XAS[83]

XRD, chemisorption and transmission electron microscopy (TEM) provides methods to determine the size of nanoparticles, but there are some limitations to these techniques. XRD needs long range order to provide good data, chemisorption experiments measure only the available surface of nanoparticles and not the supported surface. The disadvantage of TEM is that the techniques assume that the particles analyzed in one micrograph is representative for the rest of the particles in the sample, and it is also clear that as the particles are examined only from one angle, the shapes and sizes measured may be misleading. TEM is not able to detect smaller particles below 1-2 nm at best. EXAFS on the other hand, being a local probe technique, should be an excellent choice for particle size estimations. Work done by de Graaf *et al*[83] shows the possibility of relating the first shell coordination number to the size of platinum nanoparticles deposited on a zeolite, by combining chemisorption, TEM and EXAFS results. The particles were assumed spherical and the number of atoms in each particle was then computed and used to relate the number of atoms in a particle to size.

This example can be applied to other noble metals as well. The size is determined by the first coordination shell number from Figure 1.16 (right) and then multiplied by $\frac{R_{M-M}}{R_{Pt-Pt}}$ where R_{M-M} is the distance of the metal in question and R_{Pt-Pt} is the bonding distance in platinum. The particle sizes can be related to the number of atoms in the particle by Figure 1.16 (left). The metal in question must have a face centered cubic packing

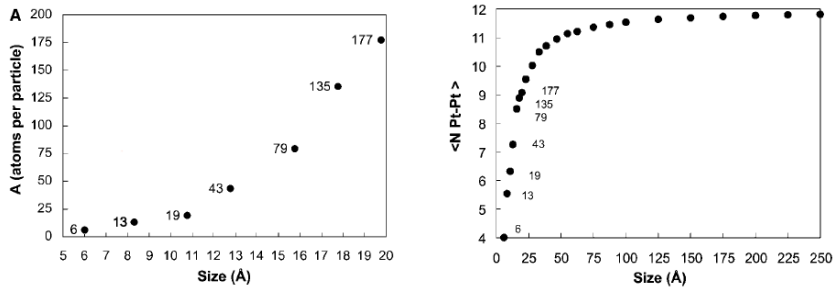

Figure 1.16: The coordination number of the i first shell related to nanoparticle sizes.[83]

and spherical particles. This method requires that the size distribution of the measured nanoparticles is narrow. If the size distribution was broad the EXAFS results would be an average of all the particles and if the size distribution was bimodal the larger particle sizes would dominate the EXAFS results.

1.7 Inductively Coupled Plasma Mass Spectrometry (ICP-MS)

Inductively coupled plasma mass spectrometry is a form of mass spectrometry where the ionized samples are atomized in the high temperature plasma source and then introduced into the mass spectrometer. ICP-MS gives the elemental composition of the introduced cationic species with detection limits down to ppb and ppt. Samples for analysis must be solubilized in water before analysis.[84,85]

1.8 Reactions theory and mechanisms[51]

Palladium is known for its ability to change between oxidation states 0 and 2+ and to form π-complexes. This has facilitated a wide variety of reactions promoting carbon carbon bond formation. Three reactions used in this thesis is Suzuki-Miyaura, Sonogashira and Heck reactions.

1.8.1 Suzuki-Miyaura and Sonogashira cross coupling reactions

These reaction couples aryl or vinyl halides with organometallic reagents and the reactions proceed in three general steps. The first step is the oxidative addition of the aryl or vinyl halide to the Pd(0), followed by the transmetallation which is the transfer of the organic group from the organometallic compound which results in a Pd(II) complex. The last step is the reductive elimination forming the product and the regeneration of the Pd(0). The palladium is usually coordinated with ligands. The ligands can regulate the product of the reactions by promoting specific stereochemistry. A general catalytic circle is illustrated in Figure 1.17.

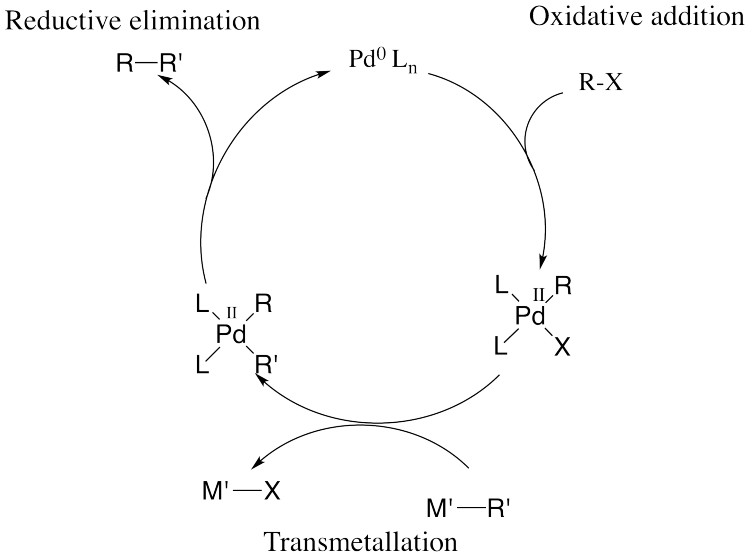

Figure 1.17: The general catalytic circle of cross coupling reactions. If the M' is Cu it is categorized as a Sonogashira cross coupling and if it is a boronic acid/ salt it is categorized as a Suzuki-Miyaura cross coupling. R group is the aryl or vinyl halide and the R' is the terminal alkyne. L is neutral ligands

A coupling between a terminal alkyne and vinyl/aryl halide or sulfonates, where copper forms the organo-alkyne is traditionally called a Sonogashira coupling. The coupling is initiated with a basic amine deprotonating the alkyne. Later experiments have shown that the reaction can be carried out without the copper and the amine, but with a carbonate salt present

instead.[51,86]

The Suzuki-Miyaura cross coupling is often referred to as the Suzuki coupling. The difference is that the *M'* is a boron compound. It can be boronc acid, boron ate esters and boranes. The reaction proceeds in a similar manner as the Sonogashira cross coupling. The addition of base is often necessary when the organoboron compound is a boronic acid. The reaction couples aryl halides, alkynyls and triflates with the organoboron compound.

1.8.2 Mizoroki-Heck reaction

The Mizoroki-Heck reaction is often called the Heck reaction.The Mizoroki-Heck reaction is a net substitution of a aryl/alkenyl halide with an alkene and the reaction can be performed with alkenes, aryl substituted alkenes, acrylate esters, vinyl ethers and N-vinylamides. The reaction does not contain the transmetallation step as the cross coupling reactions. The mechanism of this reaction has oxidative addition of the halide, and reductive elimination of the product, but there is also an insertion of the olefin forming a π-complex with the palladium complex and then forming a σ- complex resulting in a β-elimination. The reaction needs a base regenerate the catalyst. The general mechanism is shown in Figure 1.18.

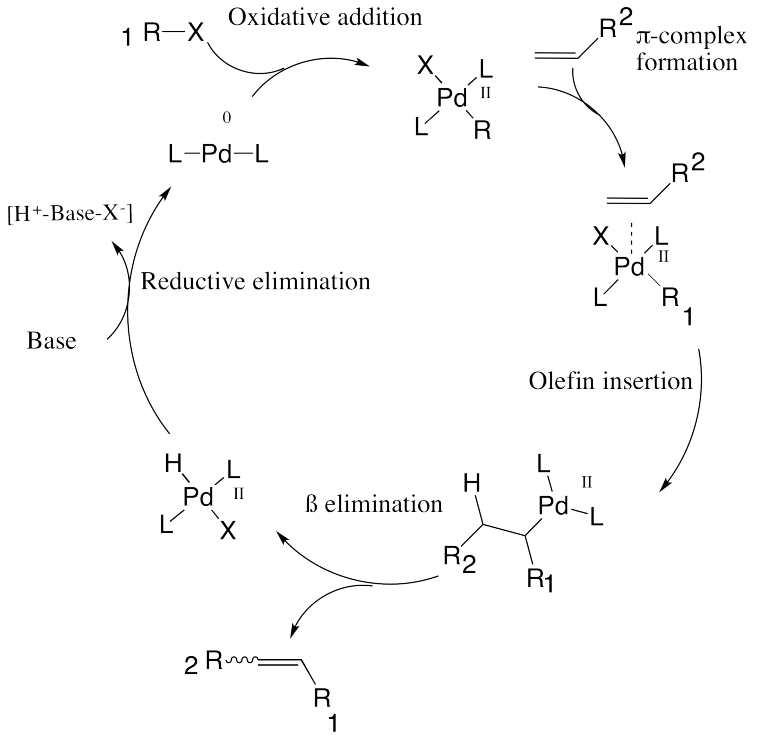

Figure 1.18: The general catalytic circle of a Heck-Reaction. The R1-X is the aryl/alkenyl halide, while the R2 may be acrylate esters. L is a neutral ligand.

Chapter 2

Experimental

2.1 Synthesis

2.1.1 Materials

All materials used in synthesis, characterization and testing was bought from Sigma-Aldrich, Fluka, VWR or Merck.

2.1.2 MOF-5

This synthesis was adapted from D. J. Tranchemontagne, *et. al.*[17]

Terephtalic acid (1.70 g,10.1 mmol) in dimethyl formamide (DMF, 130 mL) was added to $Zn(OAc)_2$ (5.67 g, 25.8 mmol) in DMF (167 mL) over a period of 15 minutes and stirred in 2.5 h, a white precipitate was observed immediately. The precipitate was separated from the supernatant and immersed in DMF (250 mL) over night. This process was repeated with chloroform ($CHCl_3$) as the solvent. The solvent was changed after 2, 3, and 7 days. The precipitated was dried *in vacuo* and 120°C for 6 hours.

2.1.3 UIO-66

UIO-66 was synthesized after the method of L. Valenzano *et. al.*[4] The synthesis of KA003 is reported. DMF (247.8 g, 3.39 mol) was mixed with deionized water (2.5 g, 138.9 mmol) before zirconium(IV) chloride ($ZrCl_4$, 2.21 g, 9.5 mmol) was added and mixed for 15 minutes. Terphtalic acid (1.67 g, 10 mmol) was added and the solution was mixed for 15 minutes. The container was sealed and heated to 120°C and let to crystallize for 24 h. A white precipitate was observed. The solvent exchange was preformed with chloroform, or 96 % ethanol. The precipitate was separated from the supernatant either by centrifugation or filtration, before the residual solvent was removed *in vacuo* at 120 °C.

Table 2.1: Synthesis of UIO-66 and the variations in the reactant ratios

Name	**Reactant ratio** ($Zr : H_2BDC : H_2O : DMF$)	**Solvent exchange**	**Separation**
uio1	1 : 1 : 1 : 1032	$CHCl_3$	Centrifugation
KA003	1 : 1 : 14 : 339	$CHCl_3$	Centrifugation
KA025-1	1 : 1 : 14 : 339	$CHCl_3$	Centrifugation
KA025-2	1 : 1 : 14 : 339	$CHCl_3$	Centrifugation
KA025-3	1 : 1 : 14 : 339	EtOH	Centrifugation
KA034	1 : 1 : 14 : 331	EtOH	Filtration
KA035	1 : 1 : 14 : 331	EtOH	Filtration

2.1.4 Preparation of tetramminegold(III) nitrate

Preparation of tetramminegold(III) nitrate $Au(NH_3)_4(NO_3)$ followed the Skibsted and Bjerrum method[87] with some modifications.

Auric acid ($HAuCl_3 \cdot H_2O$, 1.0 g, 3.3 mmol) was added to a cold supersaturated solution of ammonium nitrate (NH_4NO_3) made from distilled H_2O (70.03 g). A concentrated ammonia solution was boiled (NH_3, 25%) and the gaseous ammonia was passed through the gold solution until the pH was stabile at 7 and a white/yellow precipitate was observed. The setup of the equipment is shown in figure 2.1.4 The precipitate was washed with a cold supersaturated NH_4NO_3 solution and ethanol (96%). The precipitate

was dried in RT with ethanol when the supernatant tested negative for chloride ions in the silver nitrate ($AgNO_3$) test.

Before and during the procedure the glassware was cooled in the freezer or by ice to enhance the yield. Au^{3+} was protected from light exposure to prevent the formation of metallic gold during the procedure.

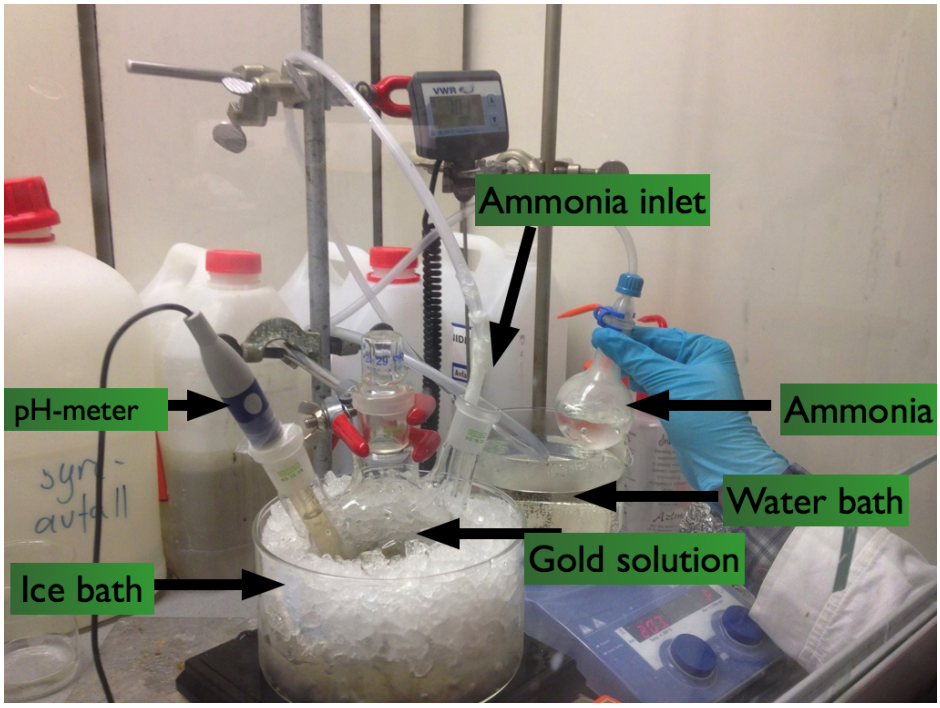

Figure 2.1: Equipment used in the formation of the $Au(NH_3)_4(NO_3)$

Preparation of gold solutions for impregnation The $Au(NH_3)_4(NO_3)/NH_4NO_3$ powder was dissolved in water or DMF. The solutions was stored at 4 °C for maximum 3 days.

2.2 Au-UIO-66

2.2.1 Impregnation / Depostion

KA008 was made by dissolving the prepared tetraaminegold(III)nitrate powder (0.45 g) in DMF (20.05 g). The gold solution (2-5 mL) was added to the support so that that it formed a thick slurry. The slurry was dried at 120 °C and the deposition process was repeated one more time. After the last deposition/impregnation the powder was immersed in chloroform and the solvent was removed *in vacuo* at 120 °C. The product was stored in a desiccator.

KA041 was made from UIO-66 (1.85 g, KA035) dispersed in a gold solution (25 mL, 0.054 $\frac{g}{mL}$, H_2O) for 48 h. The suspension was centrifuged 3 times with a new redispersion in deionized water. Before the washed product was dried in petri dishes with ethanol. All glassware was covered in aluminum foil to prevent auto reduction of the gold complex.

2.2.2 Reduction and deposition

UIO-66 (1.71 g, KA035) was added to a suspension of $Au(NH_3)_4(NO_3)$ / NH_4NO_3 (11.37 g) in deionized water (150 mL). The suspension was stirred vigorously for 15 minutes before sodium borohydride ($NaBH_4$, 0.1260 g, 33 mmol) was added and the solution changed immediately color from bright yellow to dark purple. The solution was stirred for another 10 minutes before the suspension was filtered and the remaining powder was washed with deionized water (50 mL) and ether (50 mL). The pores were evacuated *in vacuo* at room temperature for 2h. To ensure the complete removal of water the powder was freeze-dried over night.

2.2.3 Encapsulation of Au nanoparticles

The gold nanoparticles were provided by Eugenia Mariana Sandru and had a size of 7 nm and had a carotenoid stabilizing layer. Two different encapsulation batches were made by the same procedure as for the synthesis of regular UIO-66 with emptying of the pores with chloroform and

evacuation *in vacuo* at 120°C, but the water used in this synthesis contained nanoparticles. The different ratios of reactants and solvents used are presented in table Table 2.2. They are related to the amounts used in the synthesis of UIO-66 in section 2.1.3

Table 2.2: Synthesis of UIO-66 with encapsulated nanoparticles

Name	**Reactant ratio** ($Zr : H_2BDC : H_2O : DMF$)
KA021	1 : 1 : 18 : 116
KA022	1 : 1 : 14 : 339

2.3 Pd-UIO-66

The preparation of palladium particles on UIO-66 framework was adapted from the method proposed by Gao *et al.*[56]

Palladium chloride ($PdCl_2$) and sodium chloride (NaCl) were dissolved in DMF. UIO-66 was added to the solution and the suspension was mixed for 10 minutes. Hydrazine hydrate (NH_2NH_2, 35wt% in water, excess) was added dropwise. The solution was stirred for 15 minutes. The grey formed powder was isolated by filtration and washed with DMF (20 ml) and dry tetrahydrofuran (2 x 40 mL). The solvent was removed *in vacuo*. Batches KA027 (Parent batch: KA025-3) and KA032 (Parent batch not included in this thesis) were made by this method.

Table 2.3: Synthesis parameters of Pd-UIO-66

Name	**Reactants**		
	$PdCl_2$	NaCl	NH_2NH_2
KA027	0.279 g, 1.57 mmol	0.31 g, 5.33 mmol	2 mL
KA032	0.275 g, 1.55 mmol	0.292 g, 5.0 mmol	2 mL

2.4 Testing in organic synthesis

2.4.1 The synthesis of diphenylacetylene (3)

The synthesis method was adapted from Gao *et al.*[56]

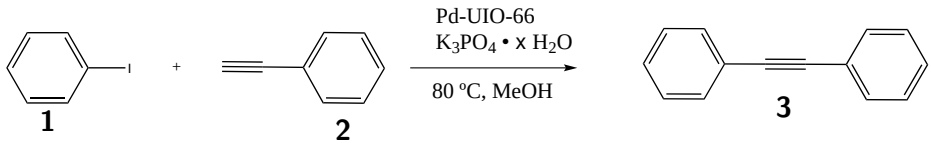

Figure 2.2: Sonogashira coupling reaction

This is an example of the synthesis of mol.diphenylacetylen. This synthesis was conducted several times with the same amounts, the only variable was the age and the environment of the catalyst had been stored under. The exact amounts used in experiment KA029 is reported.

The Pd-UIO-66 (KA027, 100 mg, 2.3wt%) and tripotassiumphosphate (K_3PO_4, 4.5 mmol, 0.955 g) was mixed vigoursly with methanol (MeOH, 20 mL). Iodobenzene, **1**, (335 μL, 3.0 mmol,) and (**2**, 360 μL, 3.3 mmol,) were added. The resulting mixture was heated to 80 °C and stirred for 3 hours. The catalyst was removed by filtration and the catalyst was washed with MeOH (2 x 10 mL). The solvent from the filtrate was removed *in vacuo*. The residue was extracted with dichloromethane (CH_2Cl_2, 2 x 20 mL) and washed with brine (20 mL). The solution was dried ($NaSO_4$) and the solvent removed *in vacuo*. The crude product was then purified by column chromatography with n-pentane as the eluent affording **3** (0.478 g, 89%) as a white powder. **Meltingpoint**: 60-61°C. **Spectroscopic properties:** ^{1}H NMR (400 MHz, $CDCl_3$-TMS): δ 7.55-7.52 (4H, m, meta-H), 7.36-7.32 (4H, m, meta-H) ppm. ^{13}C NMR (100 MHz, $CDCl_3$-TMS): δ 131.62, 128.35, 128.26, 123.29, 89.38 ppm. ^{1}H NMR and ^{13}C NMR spectra (Appendix A) are in accordance with data reported in the literature.[56]

The synthesis of **3** was conducted several times with the same amount of reactants, solvents and catalyst. The age of the catalyst was varied and also if the catalyst had been exposed to air or if was stored in inert atmosphere. The experiments are summarized in table Table 3.5. The literature reference with Pd-MOF-5 is 98% yield.[56]

Table 2.4: Synthesis of diphenylacetylene with Pd-UIO-66. KA027 was used in all of the experiments and the storage temperature was room temperature

Experiment	Age	Storage	Yield (%)
KA029	1 week	Inert atmp	89
KA031-1	1.5 months	Inert atmp	73
KA031-2	1.5 months	Ambient	35
KA033	2 months	Ambient	78

2.4.2 Synthesis of 1-(*tert*-butyl)-4-(phenethynyl)benzene (5)

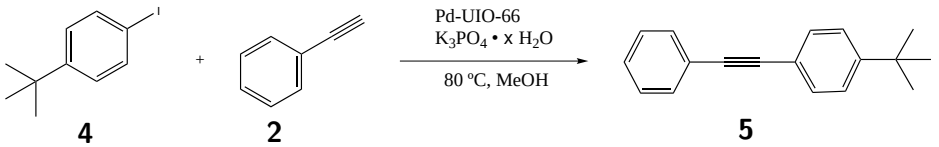

Figure 2.3: Sonogashira coupling reaction of iodobenzene derivative and phenylacetylen

K_3PO_4 (0.952 g, 4.49 mmol) and Pd-UIO-66 (KA027, 0.1025 g) was suspended in MeOH (20 mL) to give a grey suspension. 1-(*Tert*-butyl)-4-iodobenzene, **4**, (0.530 mL, 2.99 mmol) and **2** (0.365 mL, 3.32 mmol) were added. The suspension was heated to 80 °C and stirred for 3 hours. The reaction mixture was filtered and washed with MeOH (2 x 20 mL) and the solvent removed *in vacuo*. The residue was extracted with dichloromethane (2 x 10 mL) and washed with brine (20 mL). The organic phase was dried ($NaSO_4$) and concentrated *in vacuo* to give a dark brown oily phase which a white crystalline compound crystallized from when cooled. The crude was purified by silica column chromatography with n-pentane as the eluent and afforded **5** (0.296 g, 42%) as a white solid.**Meltingpoint**: 62-63°C. **Spectroscopic properties:** ^{1}H NMR (400 MHz, $CDCl_3$-TMS): δ 7.54-7.46 (4H, m), 7.38-7.30 (5H, m), 1.32 (9H, s, t-but) ppm. ^{13}C NMR (100 MHz, $CDCl_3$-TMS): δ 151.55, 131.61, 131.37, 128.34, 128.10, 125.39, 123.55, 120.28, 89.58, 88.77, 34.82, 31.22 ppm. ^{1}H NMR and ^{13}C NMR spectra (Appendix B) are in accordance with data reported in the literature.[88]

2.4.3 Suzuki coupling and synthesis of biphenyl (7)

The synthesis method was adapted from Huang *et al.*[55]

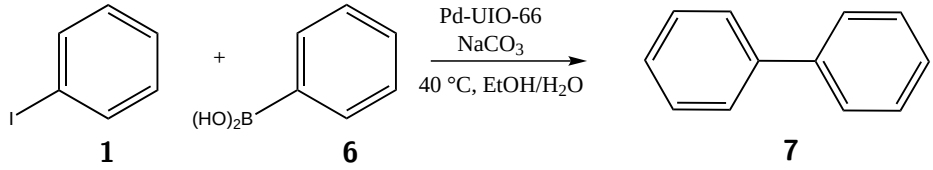

Figure 2.4: Susuki coupling reaction of iodobenzene and phenylboronic acid

In a 25 mL round–bottomed flask **1** (0.110 mL, 0.983 mmol), phenylboronic acid (**6**, 0.145 g, 1.189 mmol) and Pd-UIO-66 (KA027, 0.024 g) in water/ethanol solution (2:1, 8 ml) was mixed to give a grey suspension. The suspension was heated to 40 °C and stirred for 30 minutes. $NaCO_3$ (0.150 g, 1.415 mmol) was added and the suspension was stirred at 40 °C for another 30 minutes. The suspension was filtered through a Büchner funnel and extracted with ethyl acetate (EtOAc, 3 x 10 mL). The organic phase was dried ($NaSO_4$) and concentrated *in vacuo* to give a red brown oily phase. The crude was purified with silica column chromatography affording **7** (0.062 g,28.5%) as a white powder. **Spectroscopic properties:** ^{1}H NMR (400 MHz, $CDCl_3$-TMS): δ 7.61-7.58 (d, 4H, J_{HH}= 7.8 Hz, o-Ar-H), 7.46-7.44 (t, 4H, J_{HH}= 7.8 Hz, m-Ar-H), 7.36-7.32 (t, 2H, J_{HH}= 7.3 Hz, p-Ar-H) ppm. ^{13}C NMR (100 MHz, $CDCl_3$-TMS): δ 141.11, 128.62, 127.12, 127.04 ppm. ^{1}H NMR and ^{13}C NMR spectra (Appendix C) are in accordance with data reported in the literature.[55]

2.4.4 Synthesis of methyl cinnamate (9)

The method was adopted from Jørgensen and Gautun.[89]

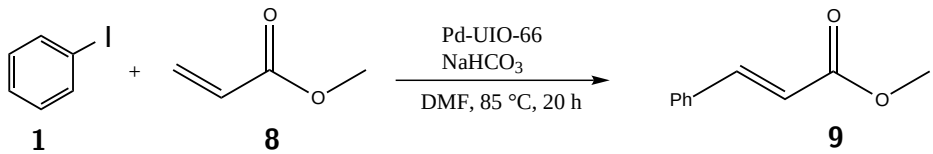

Figure 2.5: Heck reaction of methyl acrylate and iodobenzene

A Schlenk flask was charged with $NaHCO_3$ (0.401 g , 4.77 mmol) and Pd-UIO-66 (KA027, 0.415 g). The flask was evacuated and flushed with nitrogen. Iodobenzene, **1**, (0.203 mL, 1.81 mmol) and **8** (0.234 mL, 2.58 mmol) in DMF (25 mL) were added. The suspension was stirred at 85 °C for 20 hours. The suspension was filtered and the catalyst extracted with CH_2Cl_2 (100 mL) and extracted with water (30 mL). The water phase was extracted with CH_2Cl_2 (30 mL) and the combined organic fractions combined and the solvent was removed *in vacuo* which gave a red brown powder. The powder was dissolved and adsorbed on silica and the crude was purified by silica column chromatography with 5% EtOAc in n-pentane as the eluent. This afforded **9** (0.204 g, 69.4%) as a yellow white powder. **Meltingpoint**: 35-36.5°C. **Spectroscopic properties:** ^{1}H NMR (400 MHz, $CDCl_3$-TMS): δ 7.72-7.68 (d, 1H, J_{HH}= 16 Hz), 7.54-7.51 (m, 2H, m-Ar-H), 7.39-7.38 (m, 3H, o- and p-Ar-H) , 6.46-6.42 (d, 1H,J_{HH}= 16 Hz), 3.81 (s, 3H, -O-Me) ppm. ^{13}C NMR (100 MHz, $CDCl_3$-TMS): δ 167.44, 144.88, 134.40, 130.30, 128.90, 128.07, 117.81, 51.71 ppm. ^{1}H NMR and ^{13}C NMR spectra (Appendix D) are in accordance with data reported in the literature.[90]

2.4.5 Synthesis of methyl (Z)-2-((tert-butoxycarbonyl)amino)-3-phenylacrylate (11)

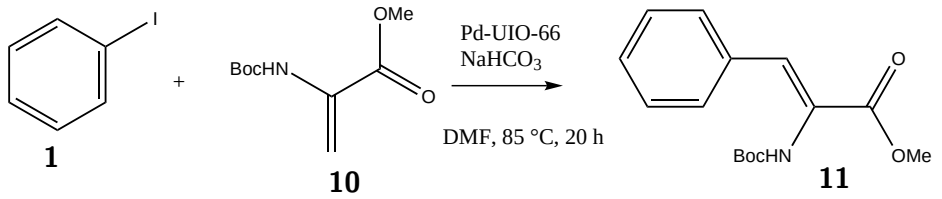

Figure 2.6: Heck reaction of 2-((tert-butoxycarbonyl)amino)acrylate and iodobenzene

The method was adopted from Jørgensen and Gautun.[89]

The Pd-UIO-66 (KA027, 0.0806 g) and $NaHCO_3$ (0.190 g, 2.26 mmol) in a roundbottomflask was evacuated. Iodobenzene, **12** (0.0405 mL, 0.362 mmol) and 2-((tert-butoxycarbonyl)amino)acrylate (100 mg, 0.497 mmol) in DMF (12.5 mL) was added to give a grey suspension. The suspension was heated to 85 °C for 20 hours. The reaction mixture were filtrated and the catalyst washed with DCM (50 mL). The organic solution was washed

with water (15 mL) and the water phase was extracted with DCM (15 mL). The combined organic phases were dried ($NaSO_4$) and the solvent removed *in vacuo*. The residue was purified by silica column chromatography (Gradient 5% EtOAc in n-pentane to EtOAc). This afforded traces of **11** as a transparent solid. **Spectroscopic properties:** ^{1}H-NMR (400 MHz, $CDCl_3$-TMS): δ 7.54-7.53 (m, 2H, m-Ar-H), 7.38-7.29 (m, 3H, o- and p-Ar-H), 7.25 (s, 1H) 6.18 (br, 1H, NH), 3.86 (s, 3H, Me), 1.40 (s, 9H, t-but) ppm. ^{13}C NMR (100 MHz, $CDCl_3$-TMS): δ 166.08, 152.76, 134.14, 130.05, 129.69, 129.17, 128.51, 124.63 ppm.^{1}H NMR spectrum (Appendix E) is in accordance with data reported in the literature.[91]

2.5 Characterization

2.5.1 Nuclear magnetic resonance spectroscopy

The NMR-spectra were recorded with a Bruker Avance DPX400 spectrometer at 400 MHz for ^{1}H-NMR and at 100 MHz for ^{13}C-NMR. The samples were prepared by solubilization in deuterated chloroform, $CDCl_3$, with an internal standard of tetramethyl silane (TMS). The shifts were caliberated after the TMS peak which was set to 0 ppm and the $CDCl_3$ then had a shift of 7.26 ppm. Traces of impurity signal was detected in some of the samples. The signals are: silicon grease 0.07 (s) ppm, alkyl chains 0.88 (t) ppm, H_2O 1.56 ppm (s), DMF 8.02 (s), 2.96 (s), 2.88 (s) pp, and EtOAc 4.12 (q), 2.14 (s), 2.05 (s), 1.26 (t) ppm.

2.5.2 XRD

1D detector

The diffractograms recorded with a 1D detector were recorded with a Bruker D8 diffractometer with Cu Kα radiation and angle measurments from 5 °to 60 °2θ. The diffractometer operated with a constant slit opening of 0.2 mm, step size of 0.018569031 °and 0.1 s per step.

A HDPXRD line detector was utilized at SNBL with X-rays with wave length of 0.5052 Å.The diffractograms were collected from 2-20°with a

step size of 0.003°and a counting time of 100 ms per step.

2D detector

A 2D dimensional detector was available at SNBL and the exposure time of the 2D detector was 2.5 second. The energy of the X-rays was 11.4 keV. The recorded diffractograms were substracted for dark current, spots in the diffractograms were removed and the centering of the diffractogram was calibrated before the diffractogram was integrated to a 1D diffractogram. The fit2D open source software was used for this work.[92]

2.5.3 Surface measurements

BET surface area was measured for 0.1-0.8 g of sample using a Micromeritics TriStar 3000 Surface Area and Porosity Analyzer. The samples were degassed at 120 °C or 250 °C and *in vacuo* for at least 12 hours before the measurements were aquired. A filler rod was useed in the sample glasses to reduced measurment error. The adsorption and desorption isotherm were recorded with 40 points for each isotherm.

2.5.4 Inductivlely coupled plasma mass spectrometry (ICP-MS)

A High Resolution Inductively Coupled Plasma ELEMENT 2 by Thermo Electronics connected to a mass spectrometer was utilized for measuring the metal weight percent. The samples were weighed (15-25 mg) and decomposed by *aqua regia* and sonication for 1.5 hours at 80 °C before the samples were diluted to 222.2 g with deionized water. Two blank samples were also prepared for analysis.

2.5.5 X-ray absorption spectroscopy (XAS)

Data aquisition
XAS data was collected at the SNBL (BM01B) at the ESRF, Grenoble, France. The beam line spectral range is 4.9-80 keV. The detectors of the

beam line is mounted as in Figure 2.1. The first ion chamber I_0 was filled with a gas mixture of 3% Ar and 97% N_2, while I_1 and I_2 were filled with 60% N_2 and 40% Ar. Ion chamber I_0 detects the initial energy of the beam, I_1 detects the intensity of the beam after it has passed through the sample and I_2 detects the intensity of the beam after it has passed through a reference metal foil. A Si (1 1 1) double cut crystal was used as a monochromator.

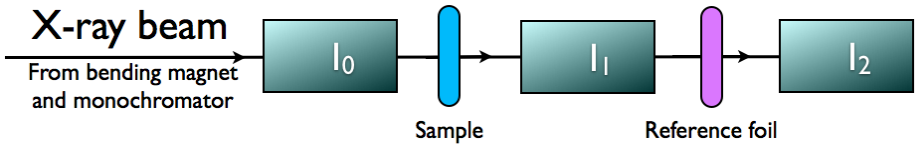

Figure 2.1: Illustration of the path of the X-ray beam in the experimental cabin and the positions of the different detectors and samples.

The data was collected in transmission mode at the gold L_{III}-edge (11919 eV) from 11.8 keV to 12.5 keV with steps of 0.5 eV and counting time of 200 ms. For samples with low concentration several scans were collected and summed to increase the signal to noise ratio. The samples were energy corrected with a Au foil (11919 eV) calibration standard. The spectra were rebinned to increase signal to noise ratio and to reduce the total number of data points. This was done by the Athena program.[93]

Sample preparation
XAS samples need to have the right amount of absorbing atoms. Samples with a high concentration of absorbers were diluted with boron nitride until an absorption jump close to 1 was achieved. To achieve good data collection of samples with low amount of absorber, it was necessary to use a higher amount of sample and thicker sample cells. *Ex situ* sample cells were made of aluminium, the samples were mounted in the cell and covered with Kapton tape. For the low concentration samples there were thicker cells.

The *in situ*-cell is illustrated in Figure 2.2. The cell was mounted in accordance with the illustration to the right in Figure 2.2 with a mica window pointed towards the beam from detector I_0 and a graphite window mounted towards detector I_1. The sample (ca 25 mg) with a particle size of 0.212-0.425 mm was placed in the middle of the cell with high temperature

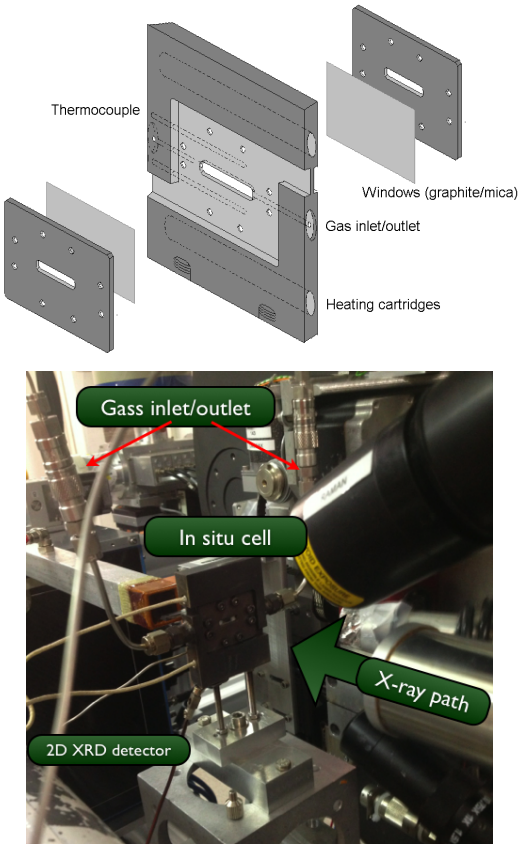

Figure 2.2: Left: Illustration of the *in situ*-cell for XAS recording. (Design and illustration by Karina Mathisen). Right: The *in situ* sample cell mounted with the 2D-XRD detector (black rectangle) in the background, after the beam has been transmitted from the sample it passes a vacuum tube to the detector.

glass wool on both sides. The gass inlet and outlet lines were connected and the gass was passed through the sample. The heating cartridges was placed above and below the sample. The heating of the cell was done with a voltage supplier, and the temperature was controlled with thermocouple feedback.

Decomposition of KA008 was studied *in situ* with the heating program illustrated in Figure 2.7. Each step there were preformed 10 EXAFS scans followed by one PXRD scan using the HRPXRD detector. KA042 was also investigated *in situ* according to Figure 2.8.

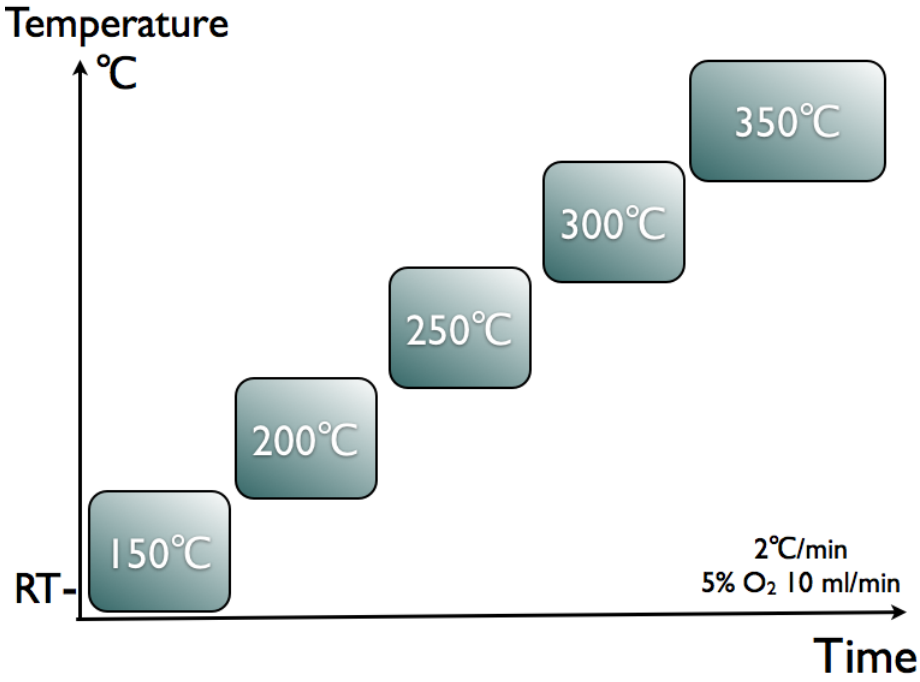

Figure 2.7: The reaction outline for the thermal stability of KA008.

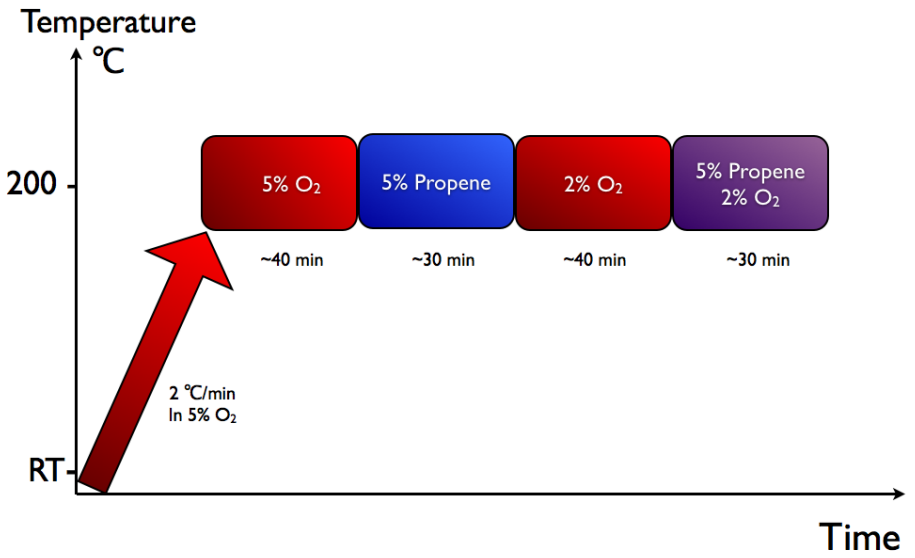

Figure 2.8: The reaction outline for testing of KA042. The gas flow through the *in situ cell* was 10 $\frac{mL}{min}$.

Data reduction and analysis

The Athena software is a plotting program for XAS data.[93] The data is plotted in intensity against energy. Athena is able to transform the energy curve to the $\chi(k)$ curve and is also able to produce the Fourier transform of the $\chi(k)$ and thereby plot the radial distribution of the scattering shells. The collected XAS spectras were loaded into the Athena software according to equation 1.6 with the I_1 as I for the sample and I_2 as I for the reference foil. The data was rebinned and merged. The data was energy corrected with the tabulated value for the gold L_{III} edge (11919 eV) and the reference foil data. The sample scan was then energy corrected by choosing E_0 to be at the first peak in the first derivative of the data. The E_0 is defined as the infliction point of the absorbtion edge. Data points with high intensity jumps that originated from defects in the monochromator was removed. If there was a lot of noise at the end of the spectrum the data was truncated to remove the noise. The $\chi(k)$ curve from equation 1.8 was obtained by using Athena's background function which estimates the absorption spectra of an atom in gas phase. k-weighting in the order of 3 was utilized. The normalization range for

XANES spectra were set to 30-150 eV and for EXAFS from 150 eV and to the end of the spectrum.

The resulting $\mu(E)$ curve was then exported to the DL_ EXCURVE software, developed by the Daresbury laboratories,[94] for EXAFS refinements. The software generates a theoretical $\chi^t(k)$ curve and fits it with the method of least squares refinement with the imported experimentally gained $\chi^{ex}(k)$. The softwares uses curved wave theory as explained in section 1.6.2 with *ab initio* calculated phase shifts and backscattering amplitude for the defined atoms. Models and samples were refined with k^3 weighting. The data range in k-space was varied (Δk). First all the models were refined by keeping the coordination number, N, constant but refining the Debye-Waller factor, $2\sigma^2$, the neighbor distance, R, and the Fermi Energy E_f a correction factor to the E_0 value chosen in Athena. For the models the amplitude reduction factor, AFAC, was also refined until stable values were achieved. For the samples N, E_f, R and $2\sigma^2$ were refined until stable values were achieved. A good fit between the theoretical and experimental EXAFS curves in DL_EXCURVE is summarized in Table 2.5.

Table 2.5: Summary of different parameters indicating a probable and good fit between the therotical and experimntal curve in the DL_EXCURVE software.[a]Values above 1 is also allowed, but then AFAC is not a reduction factor anymore.

Name	**Symbol**	**Allowed value**	**Probable values**
Amplitude reduction factor	AFAC	0-1[a]	0.8-1
Goodness of fit	R(%)	0 - ∞	As low as possible
Debye-Waller	$2\sigma^2$	Positive	0.008-0.03
Coordination number	N	Positive	1-12
Distance	R	Positive	0-5

Chapter 3

Results

3.1 XRD

3.1.1 MOF-5

The MOF-5 diffractogram acquired matched the diffractogram provided by D. J.Tranchemontagne *et al.*[17] This confirmed the microstructure. The narrow peaks indicate a high degree of crystallinity.

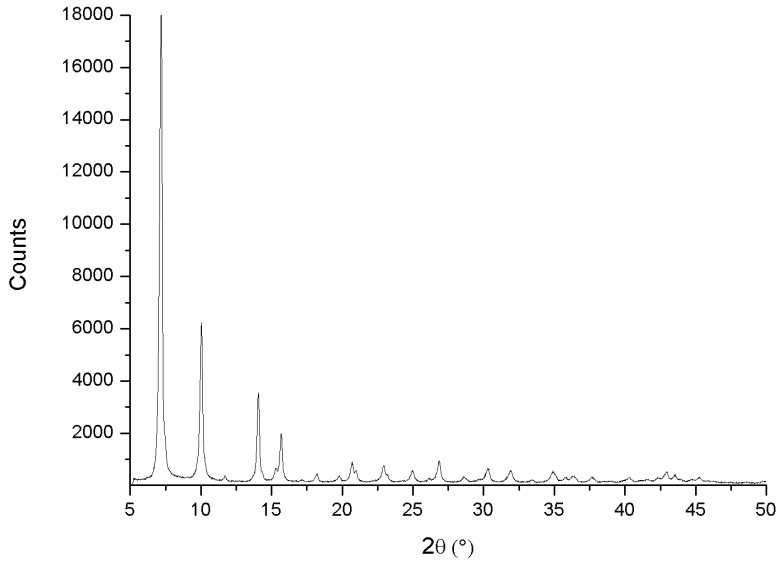

Figure 3.1: The diffractogram of the synthesized, guest exchanged and dried MOF-5from $Zn(OAc)_2$ and therephtalic acid.

3.1.2 UIO-66

The UIO-66 synthesis was performed with two different compositions. The diffraction pattern of uio1 and KA003 in Figure 3.2 is recorded with the same program and the 100% peak for KA003 is higher than the 100% peak of uio1. The height of the peaks indicates crystallinity. The crystallinity of the KA034 and KA035 is similar and shows the reproducibility of the method.

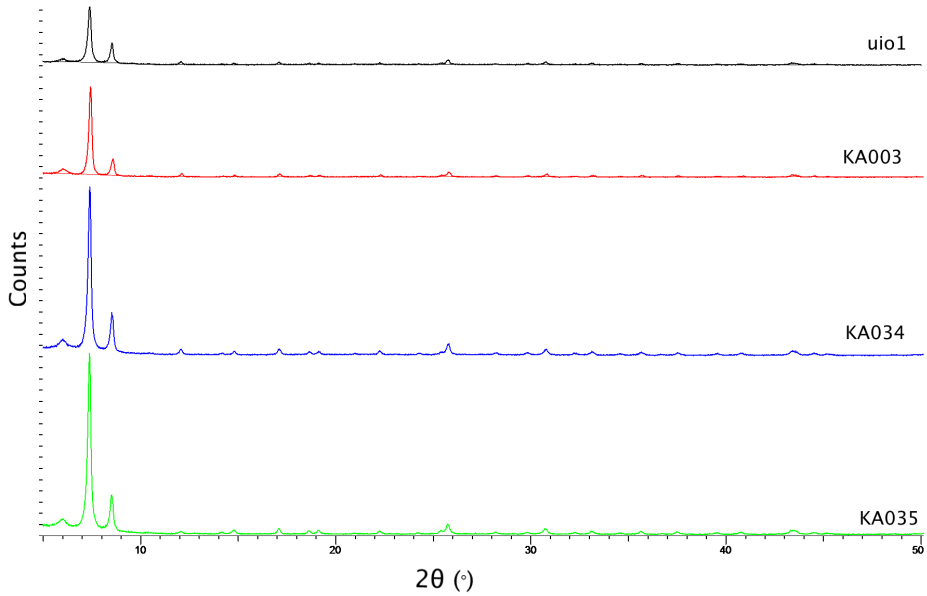

Figure 3.2: The diffractograms of the synthesized, guest exchanged and dried UIO-66 from $ZrCl_4$ and therephtalic acid.

The XRD patterns of the KA025 series may indicate that the type of solvent used for solvent exchange is not critical for the microstructure of UIO-66 as the intensity of the 100% peak varies independently of the solvent used for removing DMF from the pores.

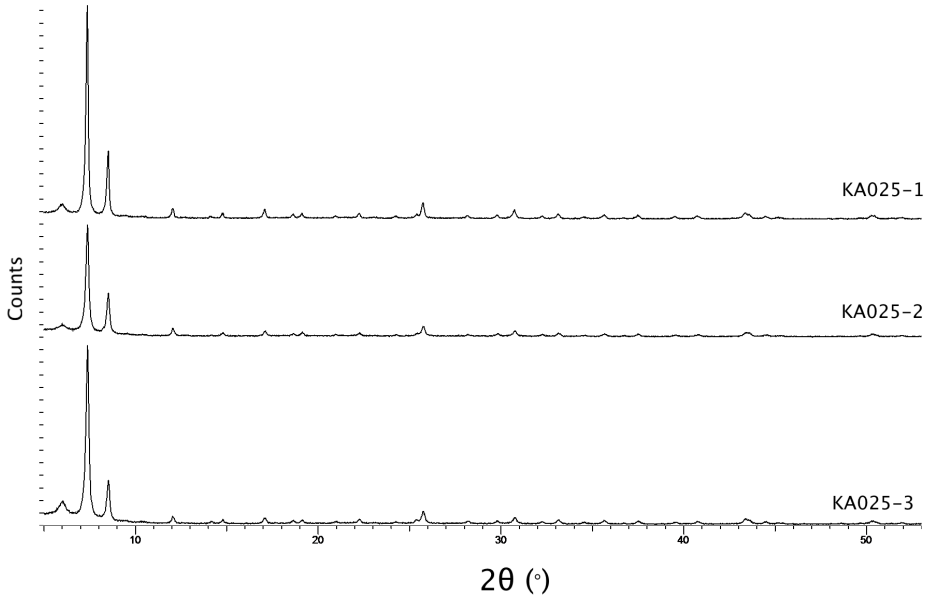

Figure 3.3: The diffraction patterns of KA025 series. KA025-1 and KA025-2 was solvent exchanged with chloroform, while KA025-3 was solvent exchanged with 96% ethanol

3.2 Surface measurments

3.2.1 BET surface area

The BET surface measurements are summarized in table Table 3.1. Degassing temperature varied between 120 °C and 250 °C to prevent agglomeration of metal particles at higher temperatures and to observe if the evacuation of the pores was complete.

Table 3.1: Results of the BET Surface area measurements. The surface area of the Au and Pd- deposited UIO-66 is included in the table.

Sample	**Specific surface area** ($\frac{m^2}{g}$)	**Degass Temperatur** (°C)	**Framework**
MOF-5	2022	120	MOF-5
KA003	731	120	UIO-66
KA008	635 [a]	120	Au-UIO-66
KA025			UIO-66
-1	640	120	
-2	599	120	
-3	781	120	
KA027	343	120	Pd-UIO-66
KA032	478	120	Pd-UIO-66
KA034	574	250	UIO-66
KA035	978	250	UIO-66

[a] Measured after 1.st impregnation

According to literature the surface areas measured in this thesis are lower than the already reported surface areas. The surface area is dependent on solvents in the pores, unreacted terepthtalic acid, interpenetrating networks and by-products such as ZnO_2 or ZrO_2. This may be due to the lowered temperature during the degassing process resulting in not a complete removal of all the solvent molecules from the pores. The observed rise in surface area with an increase in the degassing temperature supports this. There seems to be no consistency in the type of solvent and surface area.

It is also observable that the surface area is lowered when the Pd nanoparticles are deposited on the framework for the batches KA027 and KA025-3, as illustrated in Figure 3.4. The cause of this lowering might be that the particles are deposited in the pores and reduces the available surface area for adsorption measurements.

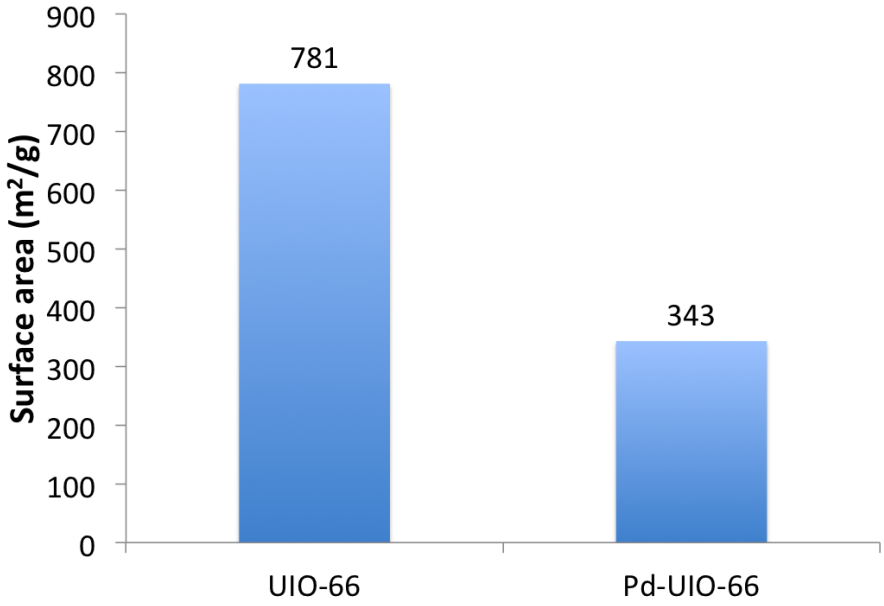

Figure 3.4: The BET surfaces of UIO-66 (KA025) and Pd-UIO-66 (KA027) with the respective micropore surface and external surface.

3.2.2 Adsorption isotherms

The adsorption isotherm can tell us something about the pores. The adsorption isotherms of MOF-5 and KA003 are illustrated in Figure 3.5, while KA025-3 and KA027 are illustrated in Figure 3.6. MOF-5 does show an adsorption isotherm similar to Type I with a hysteresis loop typical for small slit like pores while KA003, KA025-3 and KA027 has an isotherm of Type IV with a narrow hysteresis loop indicating a regular porous material.

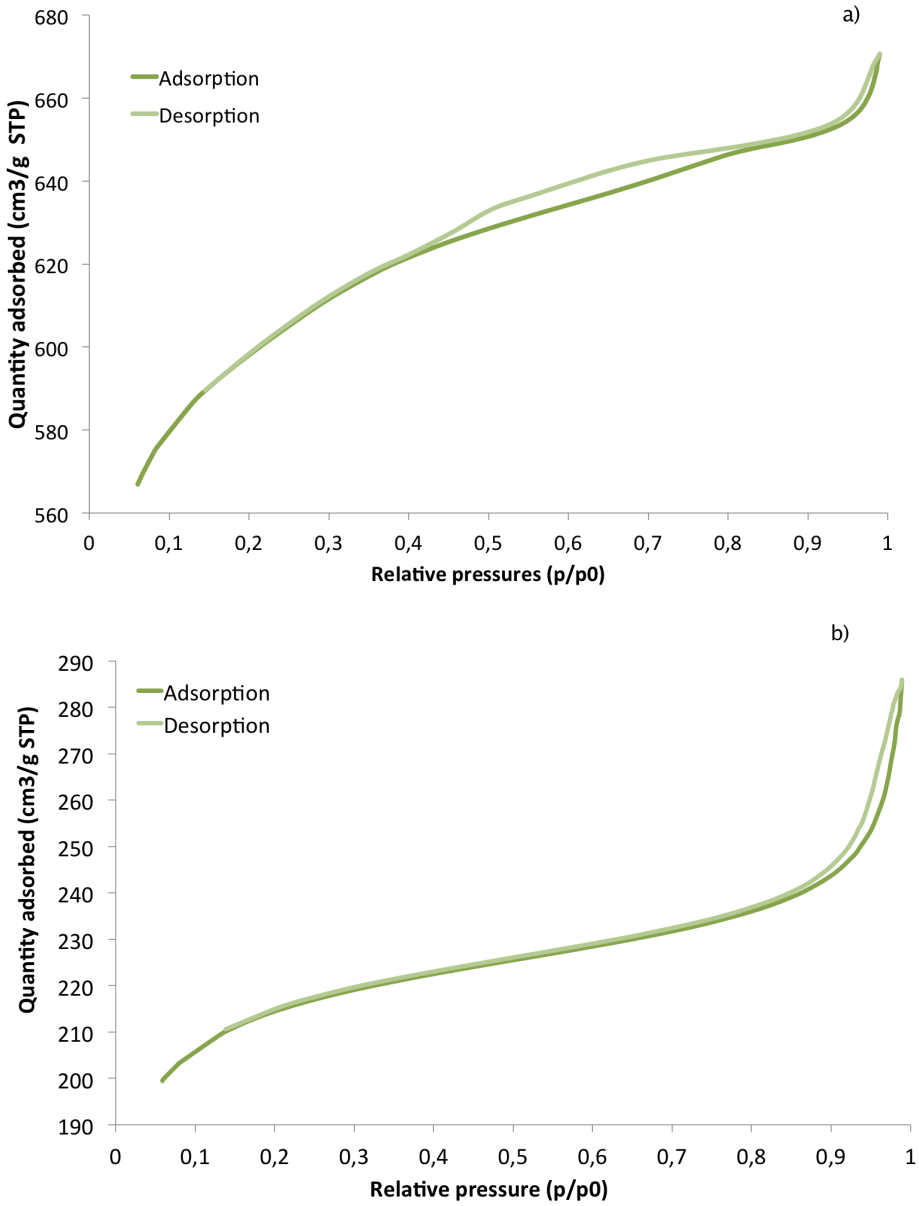

Figure 3.5: Adsorption isotherm of a) MOF-5 and b) KA003).

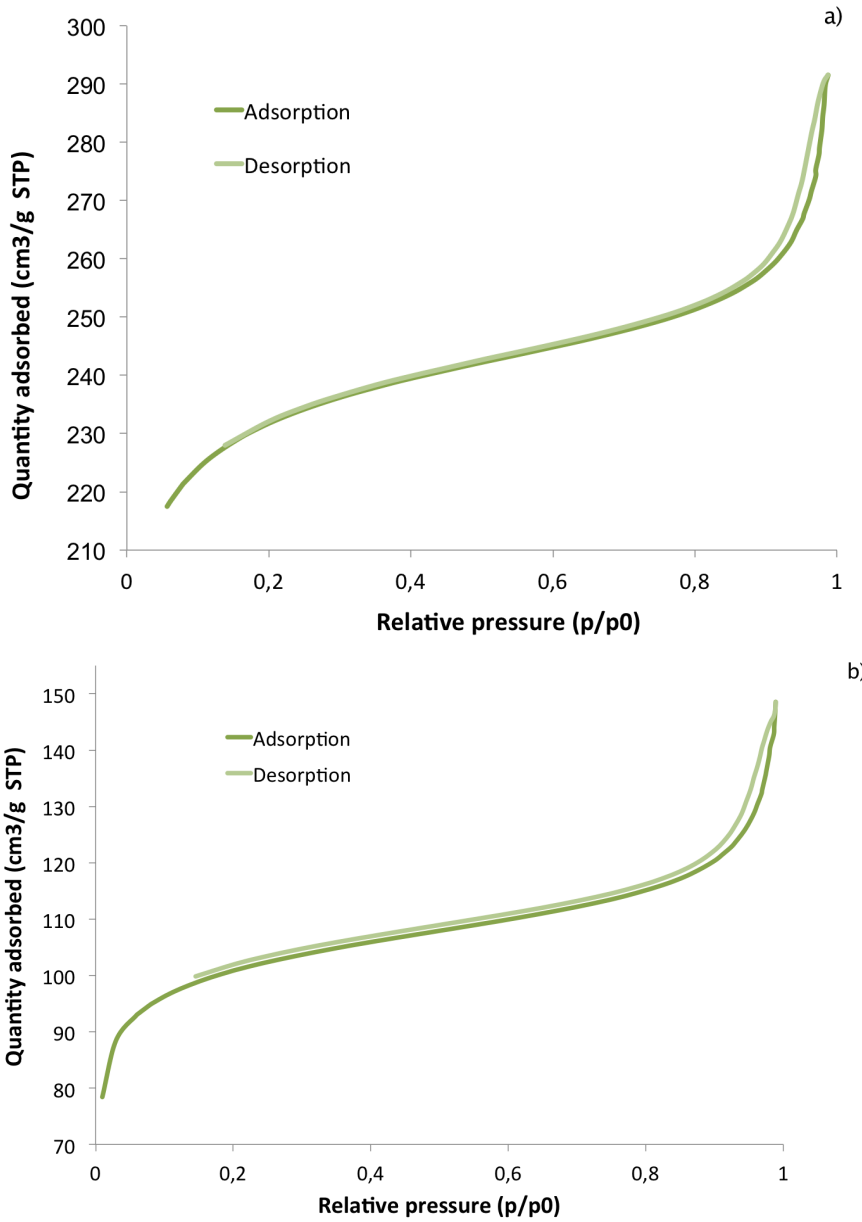

Figure 3.6: Adsorption Isotherms for a) KA025-3 and b) KA027

3.3 Inductively coupled plasma mass spectrometry (ICP-MS)

The ICP-MS results are summarized in table Table 3.2. The results shows that the uptake of metals by the impregnation/deposition method is rather low for the UIO-66. This is also the case for the encapsulation attempt. The palladium uptake of UIO-66 is higher and in line with the literature, by using an approximately solution of 0.1 wt% of the palladium precursor results in a loading of 2-3 wt%.

Table 3.2: ICP-MS results of a selection of the samples.

Sample	**Weight percent (wt%)**	
	Au	Pd
KA008	0,39	-
KA021	0,05	-
KA022	0	-
KA027	-	2,34
KA032	-	2,48

The KA021 and KA022 did not contain enough gold for further investigations and are not included in the rest of this thesis.

3.4 X-ray absorption spectroscopy (XAS)

3.4.1 Model compounds

The model compounds were a gold foil and $Au(NH_3)_4NO_3$ which represented an Au^{3+} species. The normalized XANES are shown in Figure 3.8. For the Au^{3+} species the distinct white line is present. Usually the absorption edge for ions are at higher energies than their respective metals due to an increase of the effective nuclear charge with a higher oxidation state. In Figure 3.8 this is not the case. The absorption edge of the $Au(NH_3)_4NO_3$ is shifted to lower energies. A likely explanation is that the intense white line is covering the "real" absorption edge.

EXAFS refinements were carried out on the model compounds to get a

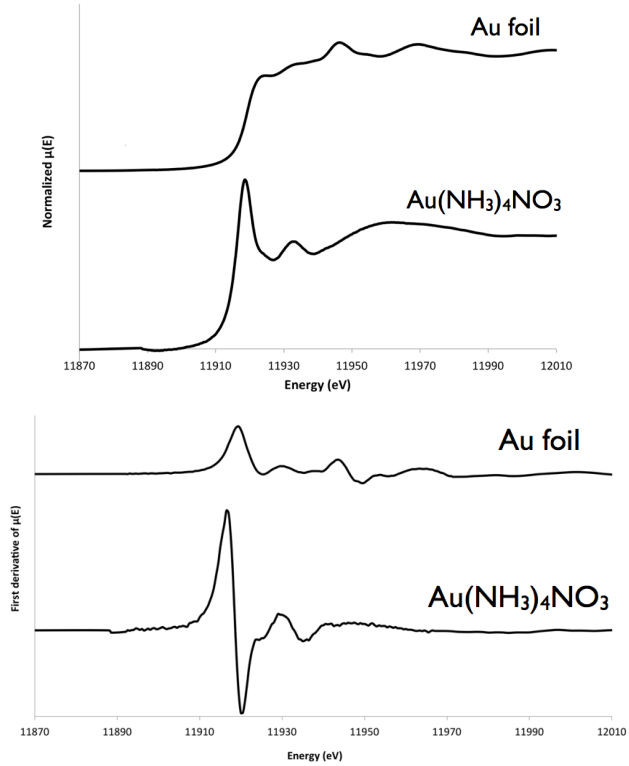

Figure 3.7: Left: The normalized XANES spectra for gold and goldtetramamine nitrate. Left. the 1 derivative of the modelcompoounds.

proper value of the amplitude reduction factor, AFAC. The refinements were done by not refining the coordination number, but refining E_F, R and Debye–Waller factor of the first coordination shell of both compounds. The results of the refinement are shown in table Table 3.3 and illustrated in Figure 3.8

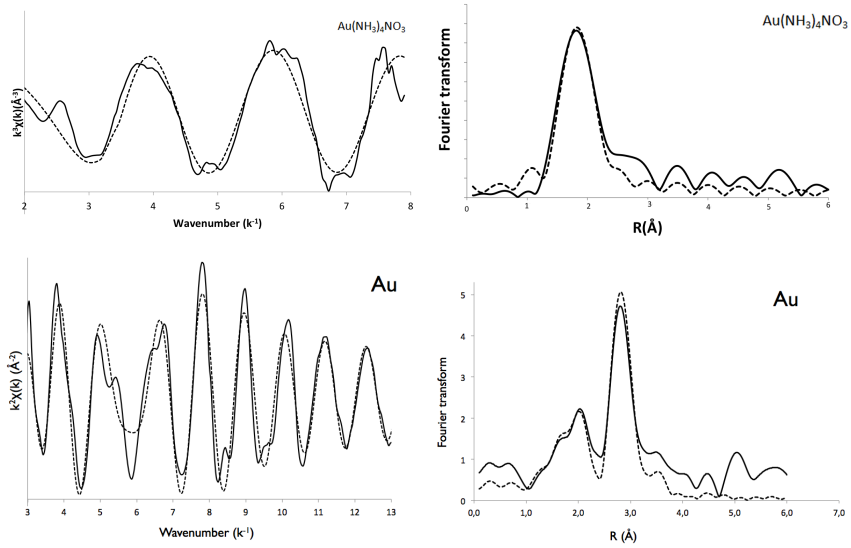

Figure 3.8: The EXAFS refinement of the AFAC, R, N, Debye-Waller and E_F results of $Au(NH_3)_4NO_3$ and the Au foil.

Table 3.3: EXAFS results for the model compounds

Model	**Shell**	**N**	**R (Å)**	**r, XRD (Å)**	$2\sigma^2$ ($Å^2$)	**AFAC**	$\mathbf{E_F}$**(eV)**	$\Delta k(Å^{-1})$	**R (%)**
Au foil	Au-Au	12	2.861(2)	2.88	0.0160(8)	0.842	-9.33	3-13	33.25
$Au(NH_3)_4NO_3$	Au-N	4	1.958(2)	2.02	0.002(5)	0.900	-6.723	2-8	33.37

3.5 Au-UIO-66

Three Au-UIO-66 were synthesized. KA008, KA041 and KA042. The former three were made with the deposition method while the latter was made with reduction of a gold solution and deposition of the gold particles. The evidence for gold in the KA042 by XRD is vague with one peak match for gold. However this peak exists in all of the UIO-66 sample so this means that it most likely is not gold that is the origin to the peak.

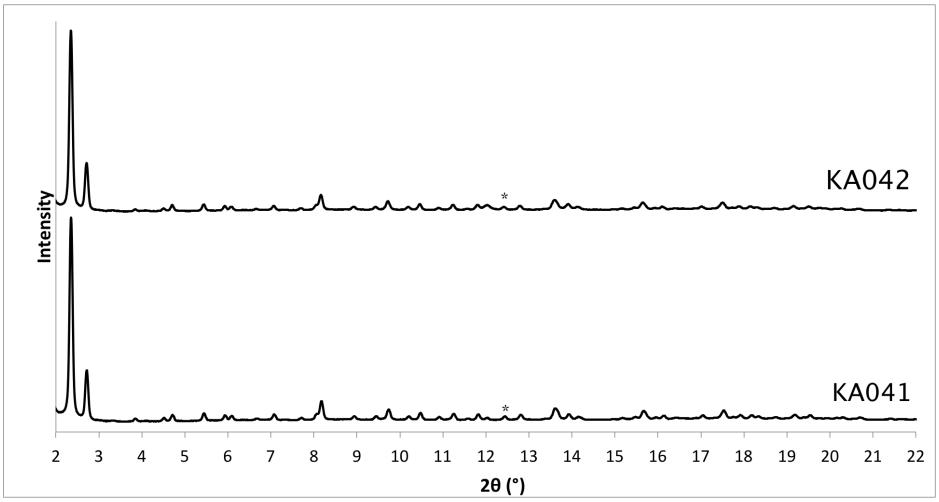

Figure 3.9: The diffraction patterns of KA041 and KA042. Note that the angles are from synchrotron radiation and with a wavelength of 0.5052 Å. The asterisk are marking a possible gold peak, but no other matches for gold was possible

KA041 sample was also investigated by XANES. The spectrum of KA041 in Figure 3.10 resemble the metallic Au foil spectra.

3.5.1 *In situ* Au-UIO-66

The thermal collapse of the microstructure of Au-UIO-66 (KA008) was observed with XRD, as seen in Figure 3.11. The decomposition of the structure is already visible from 200°C until a total decomposition at 350°C. The intensity of the 100% peak increases from room temperature to 150°C. This may be an indication of the desorption of solvents from the pores and

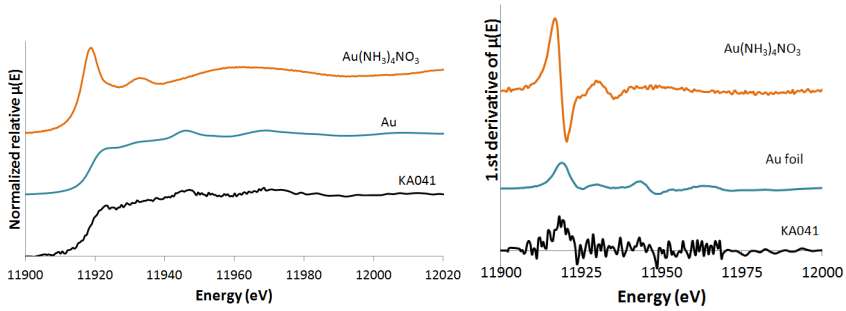

Figure 3.10: The XANES spectrum and the 1.st derivative of the of the $\mu(E)$ for KA041.

the formation of the desolated UIO-66 framework causing a higher degree of crystallinity because of structure relaxation.

XAS on the L_{III} edge of gold revealed gold in the sample. The absorption jump in energy is a measure for the concentration of the absorbing atom in the sample. An absorption jump equal to 1 is desired. The absorption jump for the gold samples are illustrated in Figure 3.12 and confirms the ICP-MS results.

Because of the low concentration of gold, several spectra were recorded which were summed to increase the signal to noise ratio. Spectra recorded during the program (Figure 2.7) revealed metallic gold in the structure and oxidation of the the metallic gold was not observed during heating in the 5% oxygen flow. The XANES spectra are illustrated in Figure 3.13.

The particle sizes of the gold particles were extracted by conducting EXAFS refinements on the recorded spectra. The quality of the data decreased by an increased in temperature. The cause of this is thermal vibrations at elevated temperatures and for samples with already low concentrations of absorber this is fatal. The decrease in quality resulted in EXAFS refinements which did not make sense. Samples recorded at elevated temperatures are therefore excluded from this thesis. The result of the pretreated Au-UIO-66 to 120°C during the preparation are illustrated in figure Figure 3.14.This resulted in the particle size of the samples already treated to 120°C as described in the experimental section. A summary of the results is in table Table 3.4.

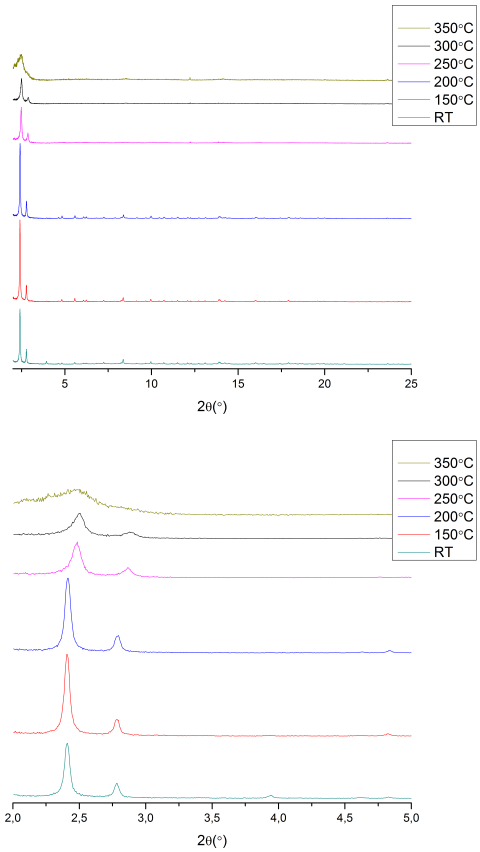

Figure 3.11: The decomposition of the microstructure of Au-UIO-66. Note: Bragg angles are given with a wavelength of 0.5052 Å.

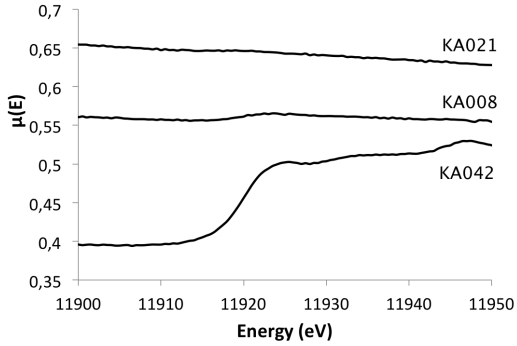

Figure 3.12: The relative jumps in the $\mu(E)$ for the samples KA008, KA042 and KA021.

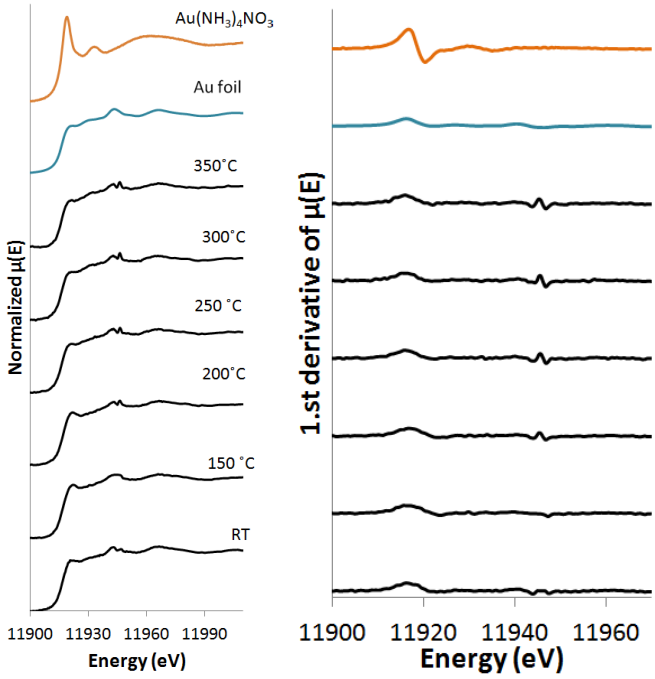

Figure 3.13: The XANES spectra of KA008 during the temperature programmed collapse. The feature at 11940 eV is a glitch in the spectra. The glitch is visible in both the XANES spectra and the 1.st derivative.

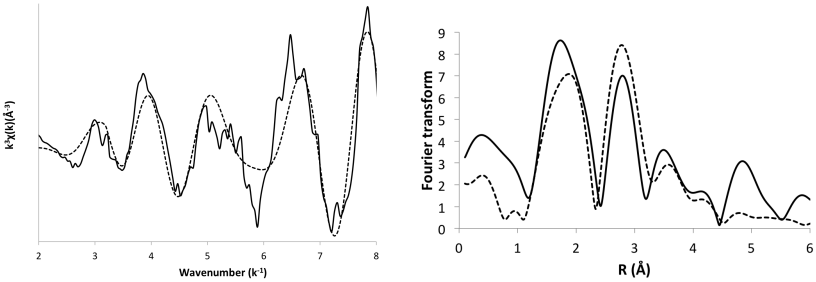

Figure 3.14: The EXAFS refinement result for KA008. The theoretical fitted curve are given as a dotted line.

The KA042 sample represents a sample made by a reduction method. The gold loading here is greater and this was confirmed by a more satisfactory absorption jump at the L_{III} edge for gold. The oxidation state was confirmed to be 0 by the lack of the intense white line in the XANES spectra as seen in Figure 3.15. The sample was not affected by a treatment of 5% O_2. There seems to be no change in the oxidation state during the different treatments of propene, oxygen or both.

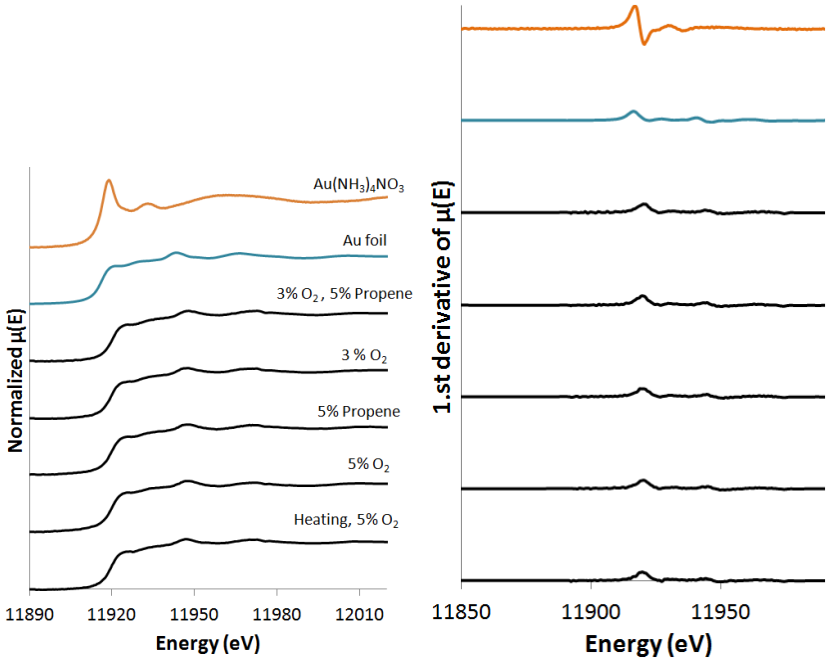

Figure 3.15: The XANES spectra of KA042 during the different treatments in Figure 2.8.

The EXAFS refinement of the spectra obtained at ambient temperature are illustrated in Figure 3.16 and the EXAFS refinements are summarized in table Table 3.4. The Δk is bigger in this refinement because the data quality was increased due to the higher concentration of the absorber in the sample.

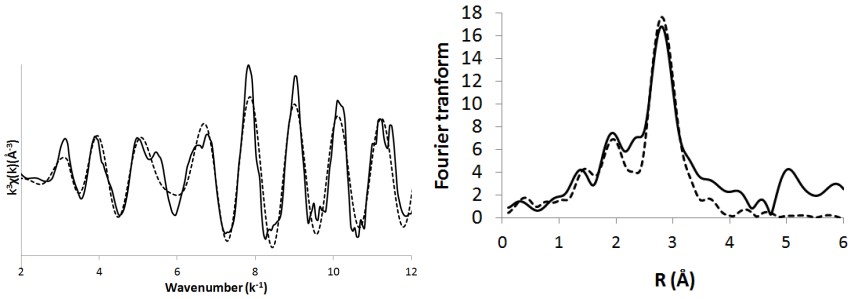

Figure 3.16: The EXAFS refinements of KA042 in room temperature. The dotted line is the theoretical fitted curve.

Table 3.4: EXAFS refinement results for KA008 and KA042 with AFAC = 0.842.

Sample	**Shell**	**N**	**R (Å)**	$2\sigma^2$ $(\AA^2)$	$\mathbf{E_F}$**(eV)**	$\Delta k(\AA^{-1})$	**R (%)**
KA008	Au-Au	10.7	2.857(3)	0.013(6)	-9.62	2-8	46.29
KA042	Au-Au	11.9	2.849(8)	0.017(0)	-8.4(6)	2-12	36.03

3.6 Pd-UIO-66

3.6.1 XRD

The KA027 and KA032 were made by the reduction deposition and characterized wit a Cu $K\alpha$ source and at SNBL with synchrotron radiation. The Pd particles were not visible with the Cu $K\alpha$ source, but with the synchrotron the particles were visible.

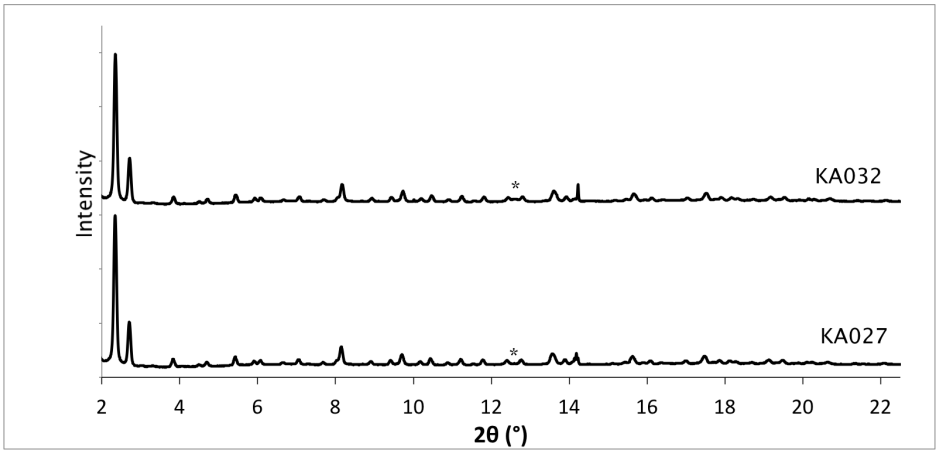

Figure 3.17: The diffraction patterns of KA027 and KA032 are recorded with synchrotron radiation with wavelength of 0.5052 Å. The asterisks are pointing out peaks that are different from the two batches.

3.6.2 Catalyzing organic reactions with Pd-UIO-66

The synthesis of **3** was conducted several times with the same amount of reactants, solvents and catalyst. The age of the catalyst was varied and also if the catalyst had been exposed to air or had been stored at -18°C or in inert atmosphere. The experiments are summarized in table Table 3.5.

Table 3.5: Synthesis of diphenylacetylene with Pd-UIO-66. KA027 was used in all of the experiments.

Experiment	**Yield** (%)	**Meltingpoint** (°C)	**Dose** (mg Pd $mmol^{-1}$ Ph-I)
KA029	89	59-60	1.08
KA031-1	73	60-62	0.84
KA031-2	35[a]	59-61	0.78
KA033	78	59-61	0.80

[a] The recovered yield.

The yield for KA031-2 is not representable and will not be discussed further. The yields of this reaction are almost consistent. The catalyst yields the most producet when it is fresh. The catalyst deactivates to lower yields

after a while, and there seems to be no difference in storage environment. These statements could be a guess at best and the need for more data points can not be emphasized enough.

The synthesis of **5** gave a total yield 42%. This experiment was conducted to indicate if the palladium nanoparticles were situated inside the pores or on the external surface. The drastic decrease in yield indicate particles inside the pores of the framework and the reactants are not able to access the particles in side the pores because of the increase in steric hindrance on **4** compared to **2**

For the Suzuki coupling reaction of **7** the reaction gave a total yield of 28,5%. After the reaction it was observed that the catalyst powder had turned black during the reaction. The black color of the sample can be caused by the palladium in the catalyst oxidizing to PdO or the agglomeration of the nanoparticles into larger deactivated particles.

The Heck reaction for making **9** had a yield of 69% and methyl cinnamate was the only detected stereoisomer. The similar reaction with **10** yielded only traces of the product **11**.

The collapse of the framework is observed after catalysis for the Sonogashira reaction, and the Heck reaction. This might be due to the work up procedure, the treatment of the catalyst during catalysis or the basic environment in the solvent.

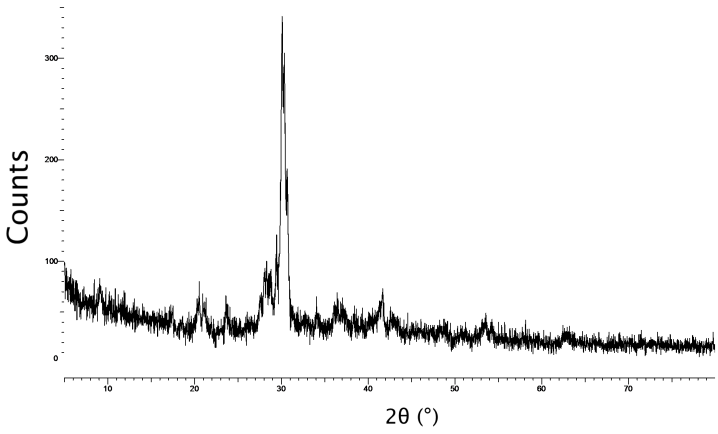

Figure 3.18: The diffraction pattern of decomposed catalyst. The peaks observed is from the residual ZrO_2

Chapter 4

Discussion

In this chapter the main goals for this Master's thesis are discussed.

MOFs have been proven as a new and exiting field of inderdiciplinary materials science, but the main challenge in the MOF-community today is to find applications for these types of materials so that MOFs seize to exist as an exciting scientific artifact. Industrial applications are crucial for the development of this field and BASF has ongoing work on MOF-5 for gas storage and supports for noble metal particles.[95] The thermal stability of MOFs is the main obstacle for this as a lot of industrial applications demand higher temperatures. The discovered UIO-66 is somewhat a breakthrough in this field with its thermal, chemical and mechanical stability. The stability is caused by the stable bond between oxygen and zirconium. Previous synthesis of MOFs is reported by Valenzano *et al*,[4] and Garibay *et al*,[70] and is done in a smaller scale than reported in this thesis. The amount of water in the other synthesis is relatively low. The amount of water is crucial for the solubility of inorganic specie, $ZrCl_4$, though the amount of water must not be too high because of the solubility of terephthalic acid and the formation of zirconyl chloride is increased. Here a 1% solution of water in DMF is used in the synthesis, and a scale up of synthesis of UIO-66 is reported. The XRD patterns obtained is phase pure as in the literature and demonstrates the flexibility of the synthesis. The surface areas reported in this thesis varies between 574-978 $\frac{m^2}{g}$ in contrast to 1064 $\frac{m^2}{g}$ and 1110 $\frac{m^2}{g}$ reported by the Valenzano, and

Geribay groups. Hafizovizc *et al.*[30] demonstrated that MOF-5 with different surface areas was caused by interconnected frameworks, remaining solvent in the pores and unreacted terephtalic acid/ inorganic species in the pores. The most probable explanation for the alternating surface area in this case is the evacuation process, as it were observed a higher surface area for higher temperatures during the evacuation. The pores could be evacuated more efficiently by using higher temperatures or more advanced methods as supercritical processing suggested by Farah *et al.*[18]

4.1 Nanoparticles on Metal-Organic frameworks

Different methods exist for making noble metal catalysts on various supports. There are several methods in use for deposition of gold onto surfaces. Usually for wet chemical methods the deposition is performed with reduction of gold species in solution and the subsequent instantaneous deposition of the particles onto the surface. This was also performed with a gold tetraamine precursor onto UIO-66 and has been proven to give the highest loading as witnessed in the Figure 3.12, from the other three methods used in this thesis. This is probably by far the most popular method for gold particle synthesis.

The impregnation/deposition method of the gold tetraamine gave rather low loading levels of the gold on the UIO-66.

Usually the gold precursor is $HAuCl_4$ and in acidic solutions it is in the form of $AuCl_4^-$. It is reported for other supports that a zero potential charge (ZPC) greater than five have given good results of small nanoparticles with stabilized oxidation states of $I+$ and $III+$. Good results have been reported for ceria, zirconia, alumina, titania and magnesia. Other supports with a ZPC ~1-2 such as silica, silica alumina or tungsten oxide exhibit poor results for gold nanoparticle stabilization.corma The precursor used in this thesis formed the cationic complex of $[Au(NH_3)_4]^+$ in solution and therefore should be better stabilized on supports with a lower ZPC. The UIO-66 as mentioned in chapter 1.1.3 consist overall of carbon and ZrO_6 coordination centers that are considered more electropositive framework and would most possibly prefer an anionic gold specie. The reported loading of KA008 is similar to Müller *et al*[44] gas phase infiltration

experiments with a gold precursor. The encapsulation of gold nanoparticles was not successful and gave low loading levels. The gold nanoparticles probably suffers from the polar carotenoid coating and thereby the affinity to the linkers.

In Figure 3.13 the observed gold species showed the characteristic spectra for metallic gold and the fact that the Au^{3+} compound is reduced to nanoparticles is clear. Under this deposition the whole procedure was performed in the dark to prevent the photoreduction of gold. But nonetheless there has been a reduction of the precursor. Wei *et al.*[46] produced silver and gold nanoparticles and core shell structures with a metal organic framework similar to the MOF to the left in Figure 1.1 with Rb^+ and Cs^+ as coordination centers instead of potassium ions. The nanoparticles were formed because of hydroxide ions, homogenously distributed in the framework, reduced the precursors when the diffused into the framework. For the UIO-66 in this thesis there should be no base present in the network itself. The solvent DMF is known to form radicals with minutes of base present,[96,97] that can reduce the gold precursor. DMF and caboxylates are known to reduce Au^{3+} compounds.[98] DMF may be present in the pores because of poor solvent exchange and terephthalate may be present in the pores because of poor washing.

The catalytic ability of gold nanoparticles is much dependent on the particle size as discovered by Haruta.[41] The size of the gold nanoparticles for KA008 is determined with the graph of de Graaf,[83] and with an average coordination number of 10.7 it gives particles sizes of 33.7 nm. The KA041 sample has an average coordination number of 11.9, and the particle size of this is hard to determine because average coordination number of bulk gold metal is 12, which means that in KA041 there are a large amounts of gold atoms that are in the neighborhood of 12 other atoms and the particle size determination with EXAFS is not a suitable technique for these particles. To determine the size of the particles in KA042 other techniques such as TEM is better. The uncertainty of the EXAFS method in combination with de Graaf is necessary to be aware of. EXAFS probes all gold atoms in the sample and the signal measured is an average of the signal from all the atoms. The EXAFS fitting procedure produces also uncertainty with standard deviations when fitting several parameters at once and last the determination from de Graafs graphs is done manually and produces uncertainty. The sample KA008 do have a relative high coordi-

nation number and the consequence of this is that the size is determined from de Graafs graph in a range where the graph increases rapidly and this makes also the result uncertain. For smaller particles the shape of the particles is not spherical and the estimation of number of atoms is just an approximation. Based on the obtained sizes the particles formed are not suited for catalysis.

The reported cage sizes of UIO-66 is 11 Å, and 8 Å, with triangular windows with length of 7 Å, reported by Mendes *et al.*.[34] The size of the synthesized particles in this Master's thesis is to large too remain inside in the framework based on these cage sizes. The reported decrease in the surface area may simply be just particles clogging pores, unsuccessful removal of solvent or formed defects in the framework during the deposition process.

Pd-UIO-66

The loading of palladium resulted in a weight percent of 2.34% and 2.48% compared with the same method employed on MOF-5 done by Gao *et al*,[56] where a weight percent of 3 was reported as the loading. Loading levels reported by other methods and other MOFs are 0.3-1wt% (coprecipitation),[57] 0.5-1wt% (impregnation)[54–56] and 12-21wt% (gas phase infiltration).[31] The lower loading of UIO-66 may be explained by the lower surface area and smaller pores of UIO-66

The diffractograms of KA027 and KA032 indicates phase pure UIO-66 samples. The asterisk marks a possible palladium peak, in KA032 but not in KA027, as a broad peak with low intensity. This may indicate that the nanoparticles in KA027 are smaller than the nanoparticles in KA032 and that the nanoparticles are below the detection limit for XRD (below 5 nm). Small nanoparticles that are not detected by XRD are small enough to fit inside the pores. The surface area is also lowered for the deposited UIO-66 with palladium in comparison with the pure UIO-66. This may indicate that pores are clogged and that some of the particles reside on the external surface of the framework. Another indication of nanoparticles on the external surface is the synthesis of **5**. The compound is more sterically hindered than **3** and will be more prone to react on the palladium nanoparticles on the external surface. This may be reflected in the lowered yield of the reaction, but on the other hand it might also be that the reaction needs further optimization for this substituent on the

reactant.

Palladium nanoparticles deposited on MOF-5 have shown catalytic activity towards Sonogashira coupling reaction in Figure 2.2.[56] Pd-UIO-66 also shows activity towards the same reactions. The yield presented in this thesis is lower than the yields presented by Gao and co-workers. The main reason for this is the amount of palladium used in the synthesis. Gao *et al* has reported that loading level of 3 wt% and a dose of 1 gives the highest yield (98%) of **3** in this copper free Sonogashira coupling. The highest yields is also obtained with the highest dose in the reactions utilizing Pd-UIO-66, but not as high yields as Gao. The other reactions performed in this thesis shows that the Pd-UIO-66 may be active towards several palladium catalyzed reaction as homogenous catalysts.

Another important feature of a catalyst is the reusability. Gao *et al.*[56] reports the reusability of the Pd-MOF-5, but the crystallinity of the catalyst after catalysis is not reported. Opelt *et al* has reported that the MOF-5 decomposes after use. In this work the Pd-UIO-66 had decomposed after the work-up procedure. It is unclear if this is a result of the reaction conditions, work-up procedure or if the nanoparticles breaks down the framework. The pure UIO-66 is synthesized in DMF and washed with both non-polar solvents such as chloroform and more polar solvents such as ethanol after synthesis. It is also reported that it can handle acidic conditions, but decomposes more rapidly under basic conditions (NaOH). The solvents used during catalyst testing are methanol, DMF and ethanol/water mixtures, all of which the pure-support is stable in. The bases used during catalysis is tripotassium phosphate (K_3PO_4) and carbonates bases (Na_2CO_3, $NaHCO_3$) which are considered weaker bases than sodium hydroxide. The thermal stability of palladium impregnated MOF is reported to be lower than the decomposition temperature of the pure UIO-66, but not 1 order of magnitude. The highest temperature reached during synthesis is below the pore evacuation temperature and should not affect the collapse of the framework.

Chapter 5

Conclusion

The aim of this thesis was to produce new catalysts by deposition of nanoparticles onto the metal-organic framework UIO-66. The synthesis of the support is concluded successful and the flexibility of the synthesis was confirmed by phase pure diffractograms and similar BET surface as of already reported areas was obtained.

The deposition of gold on the framework was performed with three different methods. First by an impregnation / deposition method with gold tetramine nitrate, reduction deposition of the same gold complex and last an encapsulation of the gold particles was performed. Loading levels was obtained with ICP-MS and this showed that the encapsulation attempts had failed. The impregnation/depositttion method had comparable results with similar procedures in the literature. The reduction deposition was not analyzed by ICP-MS, but the loading levels was confirmed better by XAS by the magnitude of the absorption jump of $\mu(E)$ in comparison with the jumps for the two other samples. The oxidation state of the gold species on all of the samples was determined metallic by XANES. Further investigation and analysis of the EXAFS showed that the particle sizes were large and for the particles made by reduction deposition the EXAFS analysis was not the right method for particle size determination. The position of the particles was presumed to be on the external surface due to the large sizes of the particles since they are not able to fit in the cages of the UIO-66. It should be emphasized that EXAFS is a technique delivering a result based on an average of the sample. If there exists smaller

particles in the cages and pores these will not be detected properly due to the domination of the signal by the larger external particles. Based on this results the prepared Au-UIO-66 was concluded as unfitted for catalysis.

The deposition of palladium was successful and comparable to literature. There was made two samples of Pd-UIO-66 and where one of the samples had detectable palladium by XRD which indicated larger particles. The surface area measurements of Pd-UIO-66 showed lower surface area which indicate clogging of pores and particles on the external surface. The sample with no detectable palladium in XRD was used in catalysis and showed activity towards Sonogashira cross coupling, Suzuki coupling and the Heck reaction. The yields obtained was lower than the previously reported Pd-MOF catalysts, but the yields was dependent of the amount of palladium present during catalysis and this might be adjusted to get better yields. After catalysis the frameworks had collapsed, but it was not confirmed if this had anything to do with the catalysis itself or the workup procedure.

There has not been produced new catalysts with noble metal nanoparticle supported UIO-66.

Chapter 6

Future work

UIO-66 is an interesting framework because of it stability and further investigation of catalysis as an applications for this framework should be promoted. Future studies of gold nanoparticles in UIO-66 must consider the fact that this is a microporous system and therefore the synthesis of the nanoparticles should reflect this. With other precursors of gold or shorter deposition times. The focus on higher loading levels will also be beneficial for the powerful analytical method EXAFS. This can be improved by using linkers with more electron rich or electron poor groups. A possibility is also to increase the linker length to increase the cage size of the framework making the nanoaparticles more accessible. Recent studies of other metal-organic frameworks with atomic gold grafted on the linker itself shows promising results in catalysis. For the pure UIO-66 catalytic activity may also be embedded directly to the linker without the noble metals.

For Pd-UIO-66 the reason for decomposition after catalysis is crucial to investigate. Many of the above mentioned statements do also apply for the Pd-UIO-66 framework. Another interesting investigation of palladium gold or copper gold bimetallic nanoparticle formation inside the framework would be exciting research.

Bibliography

(1) Batten, S. R.; Champness, N. R.; Chen, X.-M.; Garcia-Martinez, J.; Kitagawa, S.; Ohrstrom, L.; O'Keeffe, M.; Suh, M. P.; Reedijk, J. *Cryst. Eng. Comm.* **2012**, *14*, 3001–3004.

(2) Atkins, P.; Overton, T.; Rourke, J.; Waller, M.; Armstrong, F., *Shriver & Atkins' Inorganic chemistry*, 5th ed.; Oxford university press: 2010.

(3) Steed, J. W.; Atwood, J. L., *Supramolecular chemistry*, Second; Wiley: 2009.

(4) Valenzano, L.; Civalleri, B.; Chavan, S.; Bordiga, S.; Nilsen, M. H.; Jakobsen, S.; Lillerud, K. P.; Lamberti, C. *Chemistry of Materials* **2011**, *23*, 1700–1718.

(5) Ranocchiari, M.; Bokhoven, J. A. v. *Phys. Chem. Chem. Phys.* **2011**, *13*, 6388–6396.

(6) Phan, A.; Doonan, C. J.; Uribe-Romo, F. J.; Knobler, C. B.; O'Keeffe, M.; Yaghi, O. M. *Accounts of Chemical Research* **2010**, *43*, 58–67.

(7) Ma, F.-J.; Liu, S.-X.; Ren, G.-J.; Liang, D.-D.; Sha, S. *Inorganic Chemistry Communications* **2012**, *22*, 174 –177.

(8) Stock, N.; Biswas, S. *Chemical Reviews* **2012**, *112*, 933–969.

(9) Smaldone, R. A.; Forgan, R. S.; Furukawa, H.; Gassensmith, J. J.; Slawin, A. M. Z.; Yaghi, O. M.; Stoddart, J. F. *Angewandte Chemie* **2010**, *122*, 8812–8816.

(10) Wang, C.; de Krafft, K. E.; Lin, W. *Journal of the American Chemical Society* **2012**, *134*, 7211–7214.

(11) Férey, G.; Mellot-Draznieks, C.; Serre, C.; Millange, F.; Dutour, J.; Surblé, S.; Margiolaki, I. *Science* **2005**, *309*, 2040–2042.

(12) Karagiaridi, O.; Lalonde, M. B.; Bury, W.; Sarjeant, A. A.; Farha, O. K.; Hupp, J. T. *Journal of the American Chemical Society* **2012**, *134*, 18790–18796.
(13) Batten, S. R., *Metal-Organic Frameworks: Design and application*; MacGillivray, L. R., Ed.; WILEY: 2010.
(14) O'Keeffe, M.; Peskov, M. A.; Ramsden, S. J.; Yaghi, O. M. *Accounts of Chemical Research* **2008**, *41*, 1782–1789.
(15) Zeolite topology resource page: `http://www.iza-online.org`.
(16) Li, H.; Eddaoudi, M.; O'Keeffe, M.; Yaghi, O. M. *Nature* **1999**, *402*, 276–279.
(17) Tranchemontagne, D. J.; Hunt, J. R.; Yaghi, O. M. *Tetrahedron* **2008**, *64*, 8553–8557.
(18) Farha, O. K.; Eryazici, I.; Jeong, N. C.; Hauser, B. G.; Wilmer, C. E.; Sarjeant, A. A.; Snurr, R. Q.; Nguyen, S. T.; Hupp, J. T. *Journal of the American Chemical Society* **2012**, *134*, 15016–15021.
(19) Servalli, M.; Ranocchiari, M.; Van Bokhoven, J. A. *Chem. Commun.* **2012**, *48*, 1904–1906.
(20) Single-atom active sites on metal-organic frameworks., Vol. 468, 2143, Proc. R. Soc. A: 2012, pp 1985–1999.
(21) Fujita, M.; Kwon, Y. J.; Washizu, S.; Ogura, K. *Journal of the American Chemical Society* **1994**, *116*, 1151–1152.
(22) Hwang, Y.; Hong, D.-Y.; Chang, J.-S.; Jhung, S.; Seo, Y.-K.; Kim, J.; Vimont, A.; Daturi, M.; Serre, C.; Férey, G. *Angewandte Chemie International Edition* **2008**, *47*, 4144–4148.
(23) Furman, J. D.; Warner, A. Y.; Teat, S. J.; Mikhailovsky, A. A.; Cheetham, A. K. *Chemistry of Materials* **2010**, *22*, 2255–2260.
(24) Wang, J.-L.; Wang, C.; Lin, W. *ACS Catalysis* **2012**, *2*, 2630–2640.
(25) Horcajada, P.; Serre, C.; Vallet-Regí, M.; Sebban, M.; Taulelle, F.; Férey, G. *Angewandte Chemie International Edition* **2006**, *45*, 5974–5978.
(26) Horcajada, P.; Serre, C.; Maurin, G.; Ramsahye, N. A.; Balas, F.; Vallet-Regí, M.; Sebban, M.; Taulelle, F.; Férey, G. *Journal of the American Chemical Society* **2008**, *130*, 6774–6780.
(27) Huxford, R. C.; Rocca, J. D.; Lin, W. *Current Opinion in Chemical Biology* **2010**, *14*, 262 –268.
(28) Eddaoudi, M.; Li, H.; Yaghi, O. M. *Journal of the American Chemical Society* **2000**, *122*, 1391–1397.

(29) Rowsell, J. L. C.; Millward, A. R.; Park, K. S.; Yaghi, O. M. *Journal of the American Chemical Society* **2004**, *126*, 5666–5667.
(30) Hafizovic, J.; Bjørgen, M.; Olsbye, U.; Dietzel, P. D. C.; Bordiga, S.; Prestipino, C.; Lamberti, C.; Lillerud, K. P. *Journal of the American Chemical Society* **2007**, *129*, 3612–3620.
(31) Esken, D.; Zhang, X.; Lebedev, O. I.; Schroder, F.; Fischer, R. A. *Journal of Materials Chemistry* **2009**, *19*, 1314–1319.
(32) Huang, L.; Wang, H.; Chen, J.; Wang, Z.; Sun, J.; Zhao, D.; Yan, Y. *Microporous and Mesoporous Materials* **2003**, *58*, 105 –114.
(33) Phan, N. T. S.; Le, K. K. A.; Phan, T. D. *Applied Catalysis A: General* **2010**, *382*, 246–253.
(34) Mendes, P.; Rodrigues, A.; Ragon, F.; Horcajada, P.; Serre, C.; Silva, J. In *ANQUEICCE2012*, 2012.
(35) Turkevich, J.; Stevenson, P. C.; Hillier, J. *Discuss. Faraday Soc.* **1951**, *11*, 55–75.
(36) Turkevich, J; Garton, G; Stevenson, P. C *Journal of Colloid Science* **1954**, *9, Supplement 1*, 26–35.
(37) Brust, M.; Walker, M.; Bethell, D.; Schiffrin, D. J.; Whyman, R. *J. Chem. Soc., Chem. Commun.* **1994**, *0*, 801–802.
(38) Andreescu, D.; Sau, T. K.; Goia, D. V. *Journal of Colloid and Interface Science* **June 2006**, *298*, 742–751.
(39) Edgar, J.; Cortie, M. In *Gold*; CRC Press: 2009, pp 369–397.
(40) Mulvaney, P. *Langmuir* **1996**, *12*, 788–800.
(41) Haruta, M.; Yamada, N.; Kobayashi, T.; Iijima, S. *Journal of Catalysis* **1989**, *115*, 301 –309.
(42) Carabineiro, S.; Thompson, D. In *Gold*; CRC Press: 2009, pp 89–122.
(43) González-Arellano, C.; Abad, A.; Corma, A.; García, H.; Iglesias, M.; Sánchez, F. *Angewandte Chemie International Edition* **2007**, *46*, 1536–1538.
(44) Müller, M.; Turner, S.; Lebedev, O. I.; Wang, Y.; van Tendeloo, G.; Fischer, R. A. *European Journal of Inorganic Chemistry* **2011**, *2011*, 1876–1887.
(45) Moon, H. R.; Lim, D.-W.; Suh, M. P. *Chem. Soc. Rev.* **2013**, *42*, 1807–1824.
(46) Wei, Y.; Han, S.; Walker, D. A.; Fuller, P. E.; Grzybowski, B. A. *Angewandte Chemie International Edition* **2012**, *51*, 7435–7439.
(47) Lu, G. et al. *Nat Chem* **Apr. 2012**, *4*, 310–316.

(48) Bond, G. C., *Catalysis by Gold, Volume 6*; Imperial College Press: London, GBR, 2006.
(49) Corma, A.; Garcia, H. *Chem. Soc. Rev.* **2008**, *37*, 2096–2126.
(50) Liu, H.; Liu, Y.; Li, Y.; Tang, Z.; Jiang, H. *The Journal of Physical Chemistry C* **2010**, *114*, 13362–13369.
(51) Carey, F. A.; Sundberg, R. J., *Advanced organic chemistry Part B: Reactions and Synthesis*, Fifth; Springer: 2008, pp 706–739.
(52) Chorkendorff, I.; Niemantsverdriet, J., *Concepts of modern catalysis and kinetics*, 2nd ed.; Wiley-VCH: 2007.
(53) Astruc, D.; Lu, F.; Aranzaes, J. R. *Angewandte Chemie International Edition* **2005**, *44*, 7852–7872.
(54) Huang, Y.; Lin, Z.; Cao, R. *Chemistry – A European Journal* **2011**, *17*, 12706–12712.
(55) Huang, Y.; Zheng, Z.; Liu, T.; Lü, J.; Lin, Z.; Li, H.; Cao, R. *Catalysis Communications* **2011**, *14*, 27–31.
(56) Gao, S.; Zhao, N.; Shu, M.; Che, S. *Applied Catalysis A: General* **2010**, *388*, 196–201.
(57) Opelt, S.; Türk, S.; Dietzsch, E.; Henschel, A.; Kaskel, S.; Klemm, E. *Catalysis Communications* **2008**, *9*, 1286–1290.
(58) Gu, X.; Lu, Z.-H.; Jiang, H.-L.; Akita, T.; Xu, Q. *Journal of the American Chemical Society* **2011**, *133*, 11822–11825.
(59) West, A. R., *Basic solid state chemistry*, 2nd ed.; John Wiley & sons, LTD: 2000.
(60) Niemantsverdriet, J., *Spectroscopy in catalysis: An introduction*, 3rd ed.; Wiley-VCH Verlag GmbH & Co KGaA: 2007.
(61) MATTER, University of Liverpool, Resource site., `http://www.matter.org.uk/diffraction/x-ray/powder_method.htm`.
(62) International Center for Diffraction Data., `http://www.icdd.com`.
(63) Crystallography Open Database., `http://www.crystallography.net`.
(64) European Synchrotron Radiation Facility, Grenoble, France., `http://www.esrf.eu/about/synchrotron-science/synchrotron`.
(65) Willmott, P., *An Introduction to Synchrotron Radiation: Techniques and Applications*; John Wiley & Sons, Ltd: 2011, pp 1–14.
(66) Gregg, S. J.; Sing, K. S. W., *Adsorption, Surface Area and Porosity'*, Second; Academic Press, Inc.: 1982, pp 21–24.
(67) Sing, K. S. W. *Pure Appl. Chem.* **1985**, *57*, 603–619.

(68) Rouquerol, J.; Avnir, D.; Fairbridge, C. W.; Everett, D. H.; Haynes, J. M.; Pernicone, N.; Ramsay, J. D. F.; Sing, K. S. W.; Unger, K. K. *Pure Appl. Chem.* **1994**, *66*, 1739–1758.

(69) Leofanti, G; Padovan, M; Tozzola, G; Venturelli, B *Catalysis Today* **1998**, *41*, 207 –219.

(70) Garibay, S. J.; Cohen, S. M. *Chem. Commun.* **2010**, *46*, 7700–7702.

(71) Newville, M. Fundamentals of XAFS., Electronically published at http://www.xafs.org/Tutorials; University of Chicago, Chicago, IL, July 2004.

(72) Koningsberger, D.; Mojet, B.; van Dorssen, G.; Ramaker, D. English *Topics in Catalysis* **2000**, *10*, 143–155.

(73) Teo, B. K., *EXAFS: Basic Principles and Data Analysis*; Springer Berlin / Heidelberg: 1986.

(74) National Institue of standards: Attenuation Coefficients., `http://physics.nist.gov/PhysRefData/XrayMassCoef/tab3.html`.

(75) National Institue of standards: `http://physics.nist.gov/PhysRefData/XrayMassCoef/ElemTab/z79.html`.

(76) Bunker, G., *Introduction to XAFS*; Cambridge University Press: 2010.

(77) Choy, J.-H.; Kim, Y.-I. *The Journal of Physical Chemistry B* **2003**, *107*, 3348–3350.

(78) Stern, E. *Journal of Synchrotron Radiation* **2001**, *8*, cited By (since 1996)13, 49–54.

(79) Stern, E.; Sayers, D.; Lytle, F. *Advances in x-ray analysis* **1970**, *13*, 248.

(80) Sayers, D. E.; Stern, E. A.; Lytle, F. W. *Phys. Rev. Lett.* **1971**, *27*, 1204–1207.

(81) Bordiga, S.; Groppo, E.; Agostini, G.; van Bokhoven, J. A.; Lamberti, C. *Chemical Reviews* **2013**, *113*, 1736–1850.

(82) Teo, B.-K.; Lee, P. A. *Journal of the American Chemical Society* **1979**, *101*, 2815–2832.

(83) De Graaf, J; van Dillen, A.; de Jong, K.; Koningsberger, D. *Journal of Catalysis* **2001**, *203*, 307 –321.

(84) Skoog, D. A.; West, D. M.; Holler, F. J.; Crouch, S. R., *Fundamentals of analytical chemistry*; Brooks / Cole Cengage learning: 2004.

(85) Vansecasteele, C.; Block, C. B., *Modern methods for trace element determination*; John Wiley & sons, LTD: 1993.

(86) Böhm, V. P. W.; Herrmann, W. A. *European Journal of Organic Chemistry* **2000**, *2000*, 3679–3681.
(87) Skibsted, L. H.; Bjerrum, J. English *Acta chemica scandinavica series A–physical and inorganic chemistry* **1974**, *A 28*, 740–746.
(88) Moon, J.; Jeong, M.; Nam, H.; Ju, J.; Moon, J. H.; Jung, H. M.; Lee, S. *Organic Letters* **2008**, *10*, 945–948.
(89) Jørgensen, K. B.; Gautun, O. R. *Tetrahedron* **1999**, *55*, 10527 – 10536.
(90) Williams, D. B. G.; Shaw, M. L.; Hughes, T. *Organometallics* **2011**, *30*, 4968–4973.
(91) Kometani, M.; Ihara, K.; Kimura, R.; Kinoshita, H. *Bulletin of the Chemical Society of Japan* **2009**, *82*, 364–380.
(92) The fit2D software is provided by ESRF: `http://www.esrf.eu/computing/scientific/FIT2D/`.
(93) Ravel, B.; Newville, M. *Journal of Synchrotron Radiation* **2005**, *12*, 537–541.
(94) Tomic, S.; Searle, B. G.; Wander, A.; Harrison, N. M.; Dent, A. J.; Mosselmanns, J. F. W.; Inglesfield, J. E. *New Tools for the analysis of EXAFS: The DL_EXCURVE package*; tech. rep.; Council for the central Laborotory of the Reaserch Council, 2004.
(95) Mueller, U.; Schubert, M.; Teich, F.; Puetter, H.; Schierle-Arndt, K.; Pastre, J. *J. Mater. Chem.* **2006**, *16*, 626–636.
(96) Øpstad, C. L.; Melø, T.-B.; Sliwka, H.-R.; Partali, V. *Tetrahedron* **2009**, *65*, 7616 –7619.
(97) Buncel, E.; Symons, E. A. *J. Chem. Soc. D* **1970**, *0*, 164–165.
(98) Cushing, B. L.; Kolesnichenko, V. L.; O'Connor, C. J. *Chemical Reviews* **2004**, *104*, 3893–3946.

Appendixes

Appendix A

Spectroscopic data of 3

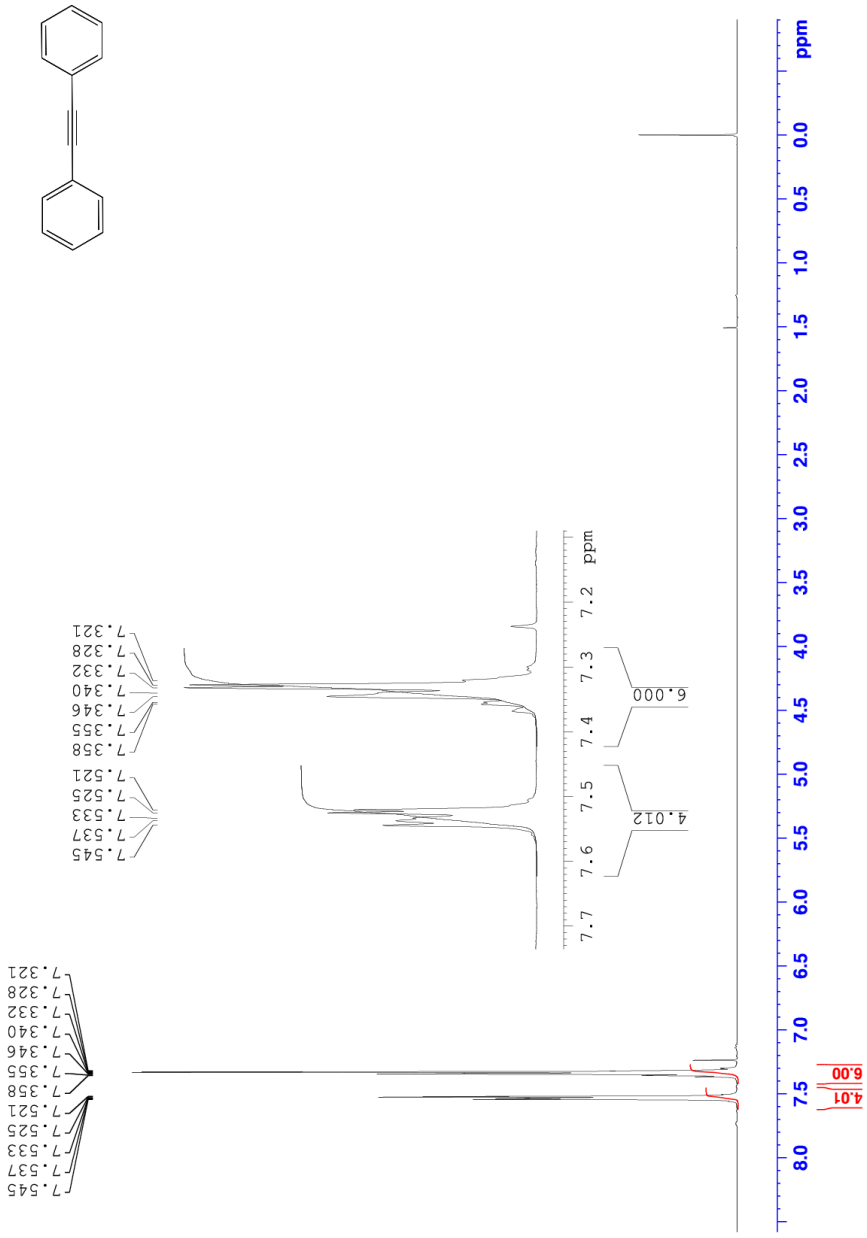

Figure A.1: The ^{1}H-NMR spectrum of **3**.

Figure A.2: The ^{13}C-NMR spectrum of **3**.

Appendix B

Spectroscopic data of 5

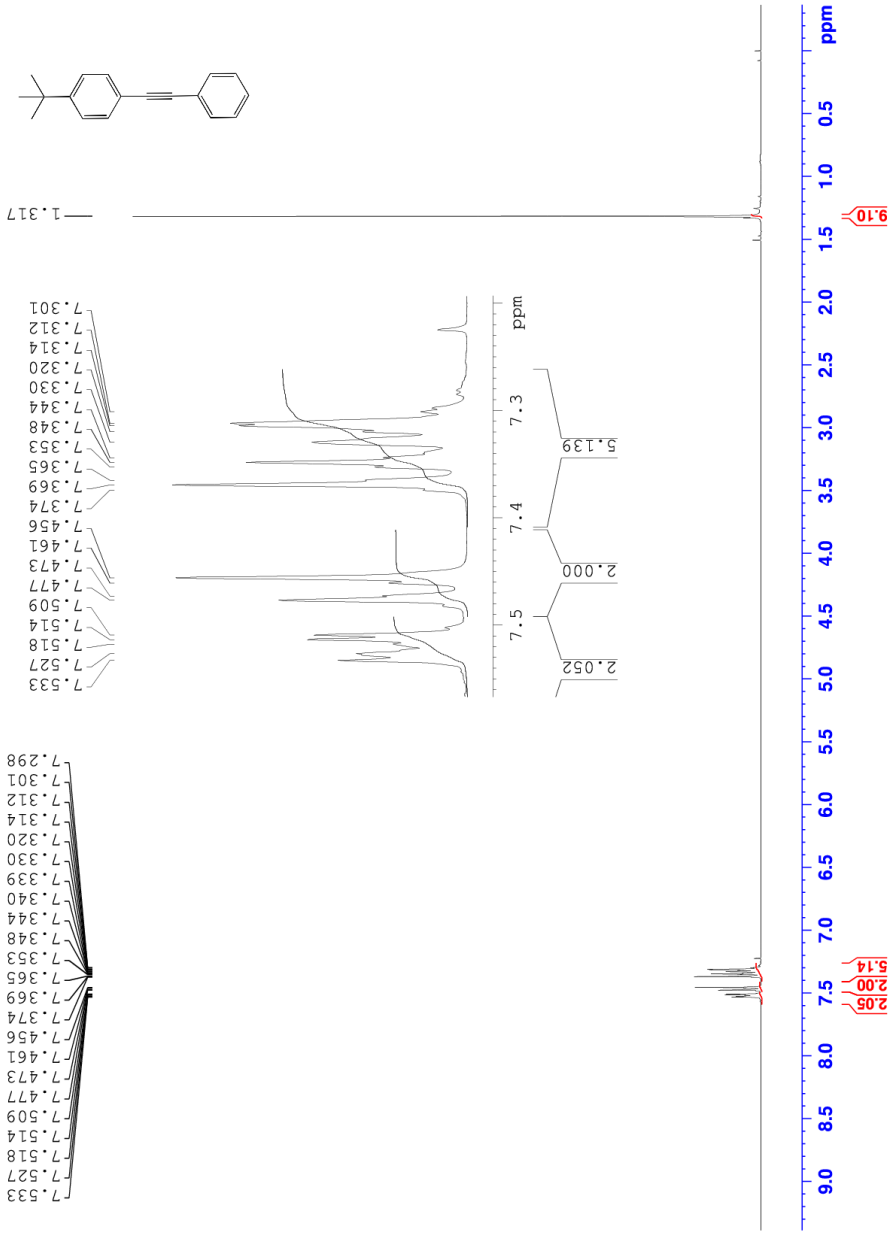

Figure B.1: The ^{1}H-NMR spectrum of **5**.

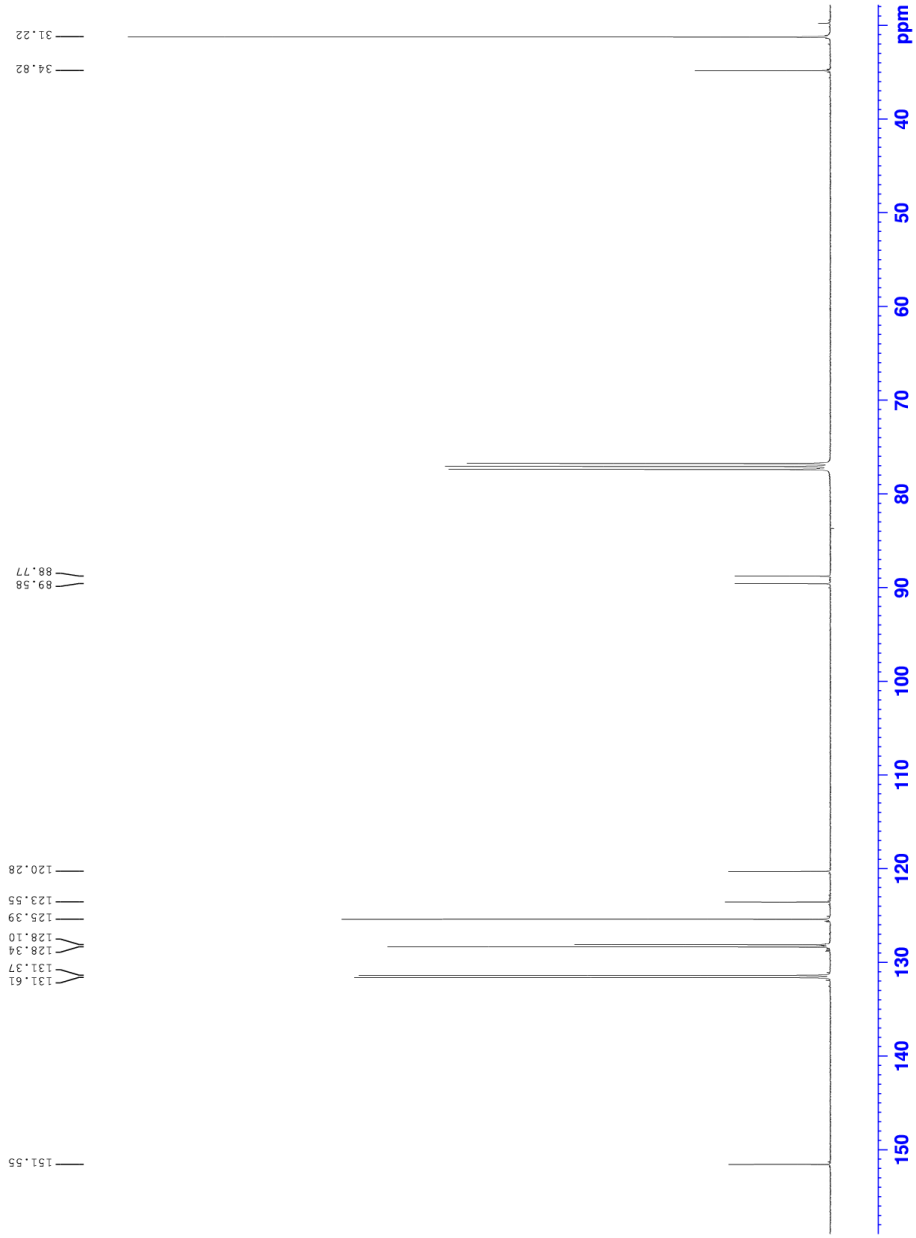

Figure B.2: The ^{13}C-NMR spectrum of **5**.

Appendix C

Spectroscopic data of 7

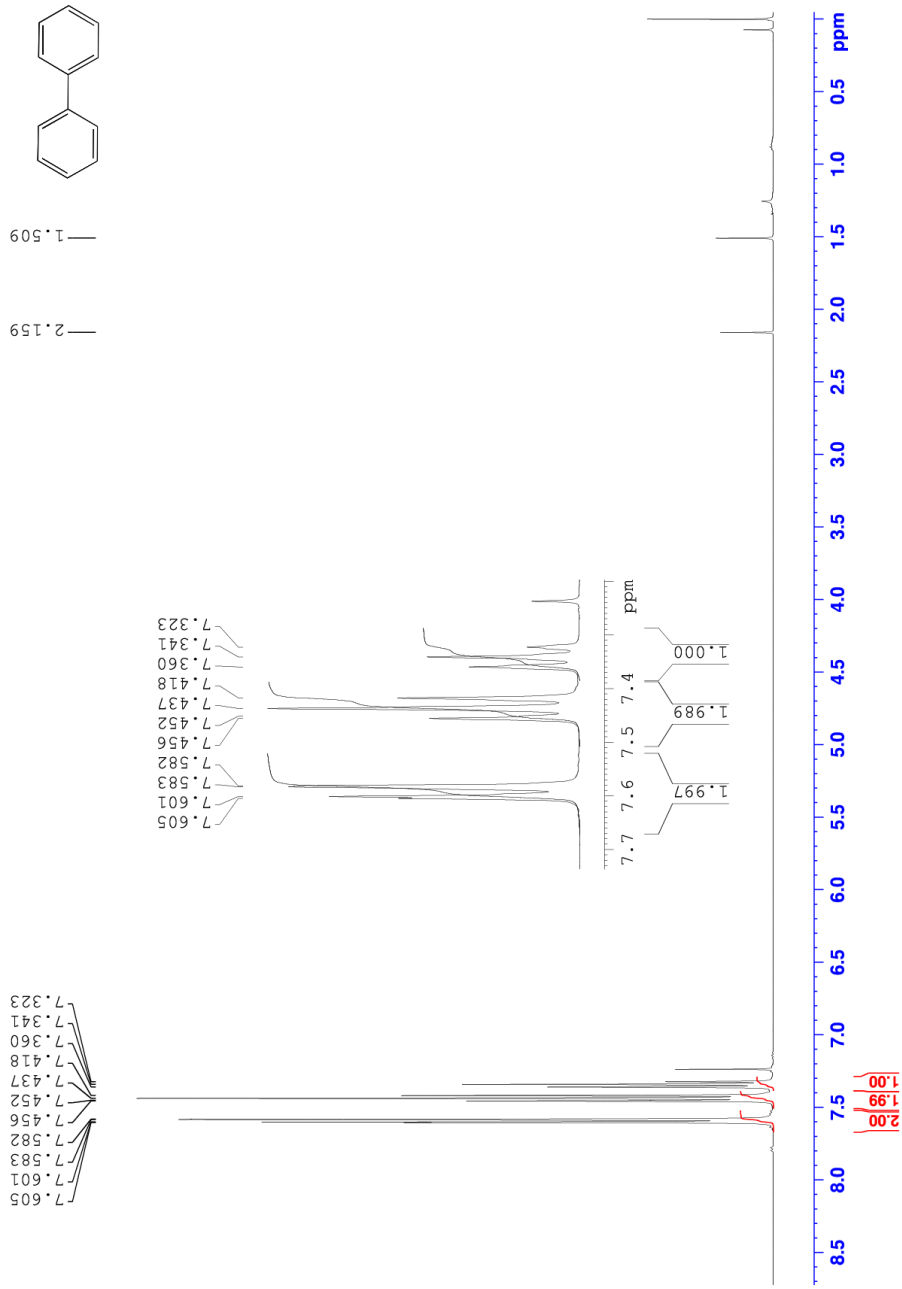

Figure C.1: The ^{1}H-NMR spectrum of **7**.

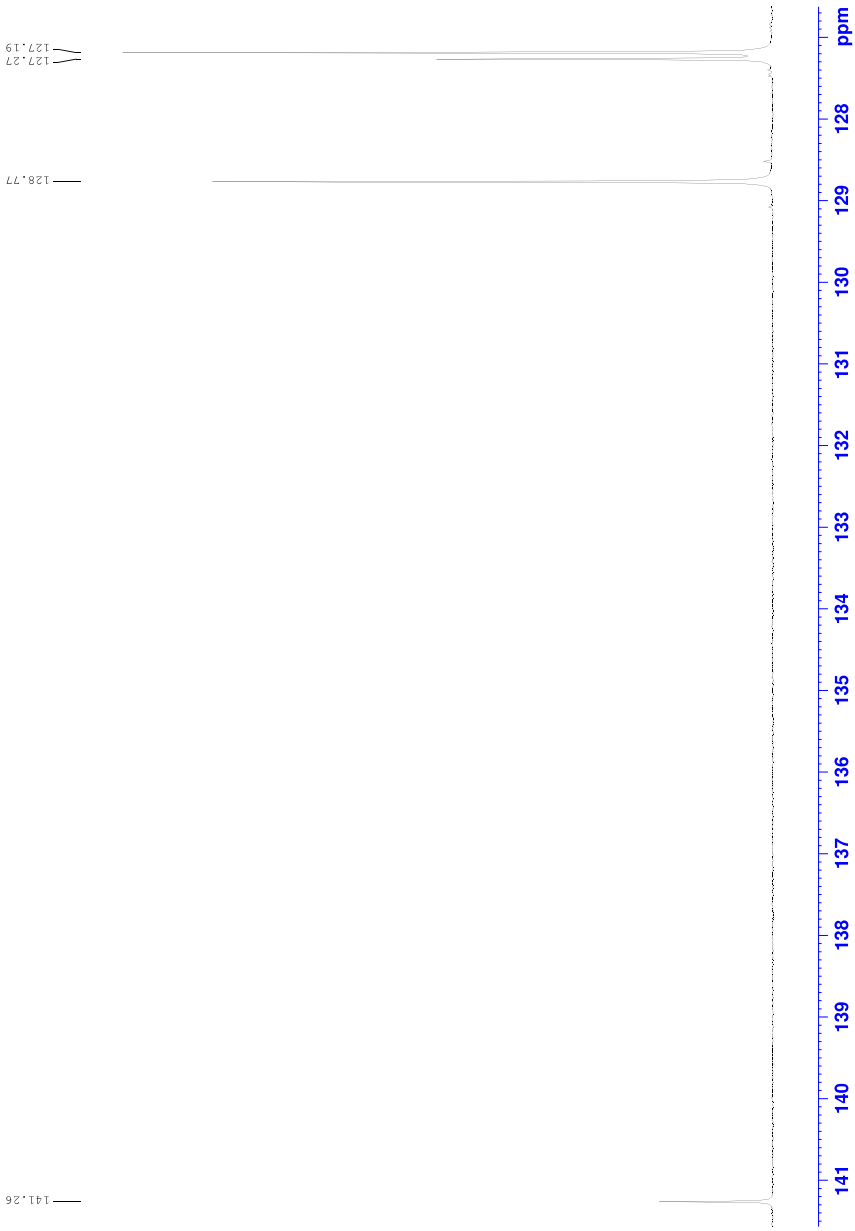

Figure C.2: The ^{13}H-NMR spectrum of **7**.

Appendix D

Spectroscopic data of 9

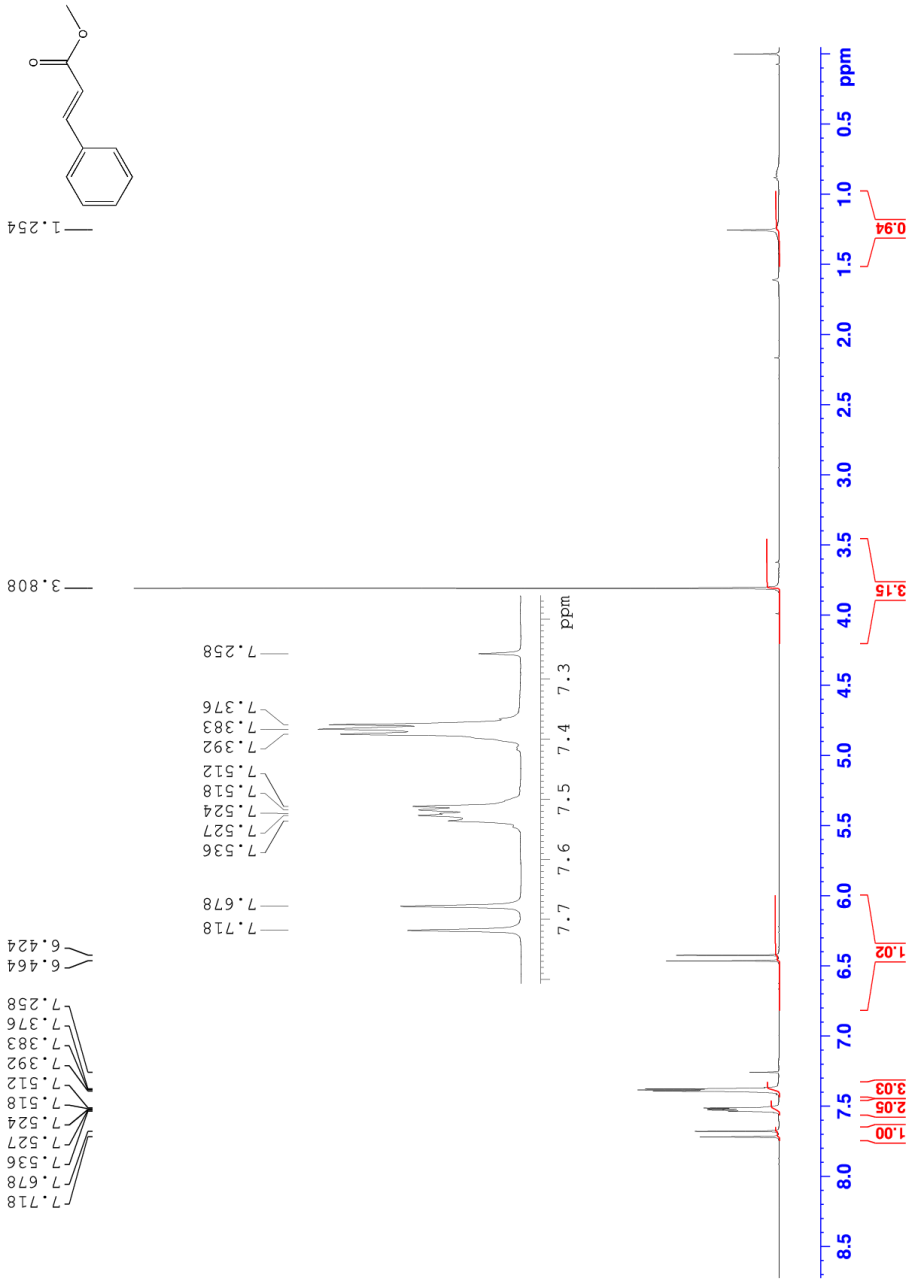

Figure D.1: The ^{1}H-NMR spectrum of **9**.

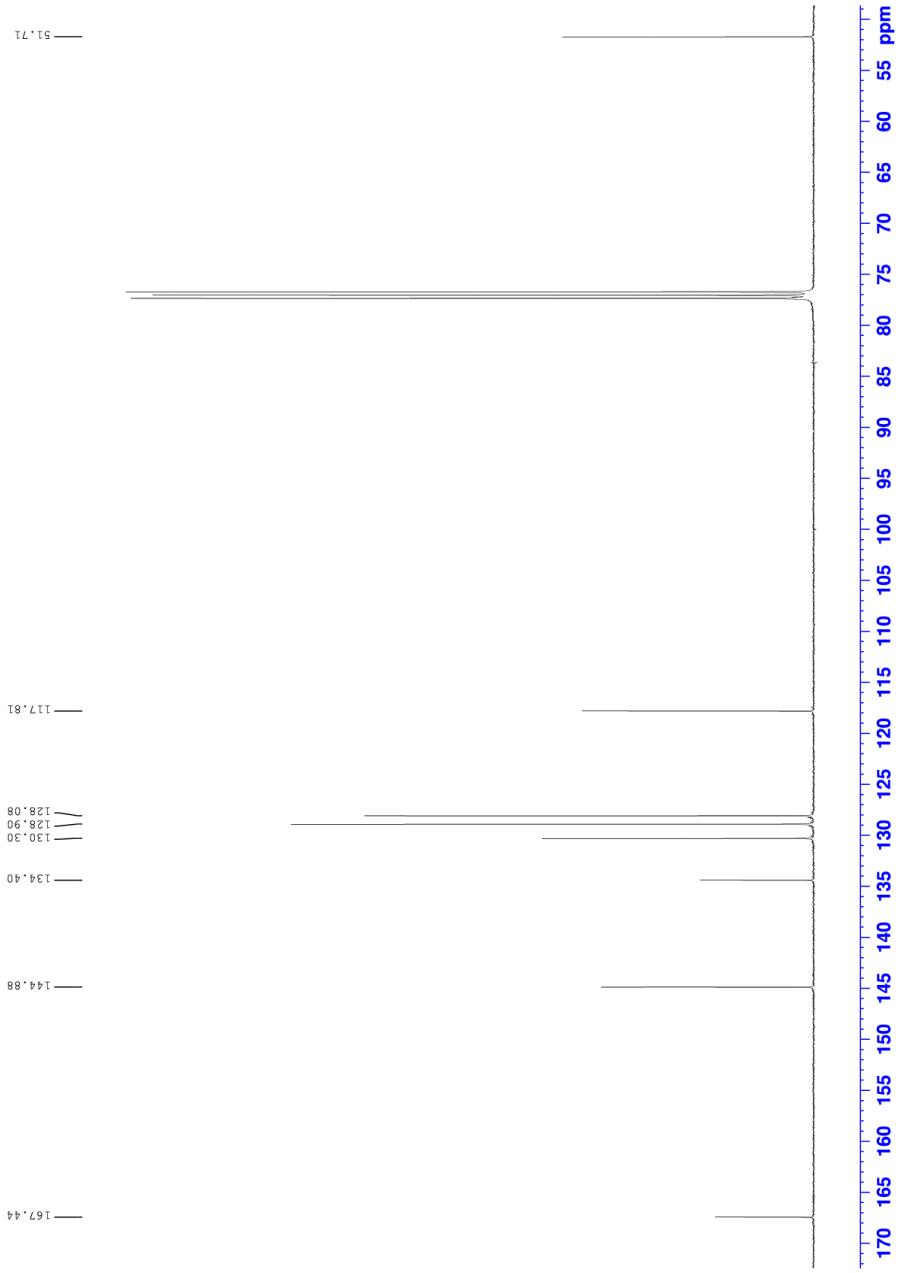

Figure D.2: The ^{13}C-NMR spectrum of **9**.

Appendix E

Spectroscopic data of 11

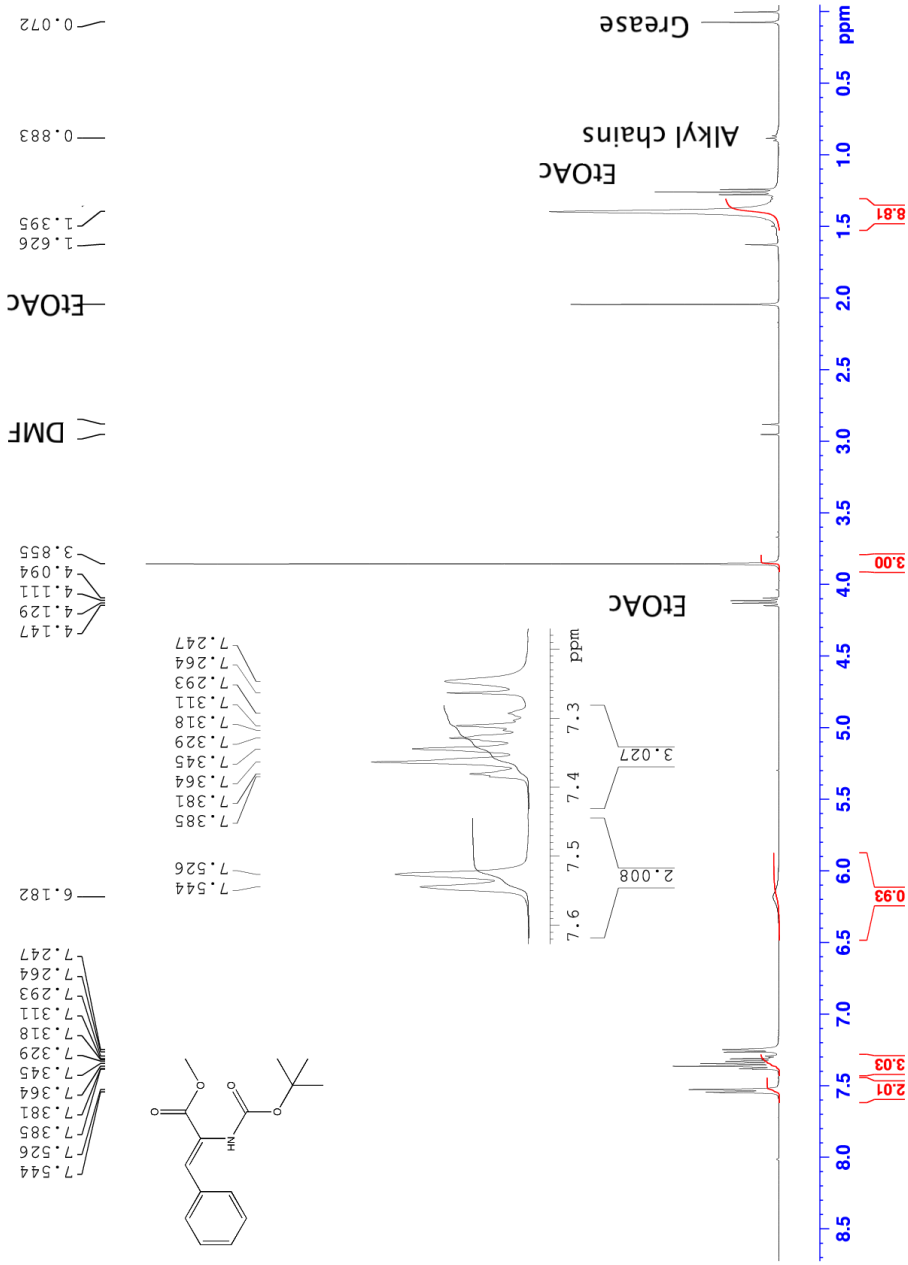

Figure E.1: The ^{1}H-NMR spectrum of **11**.

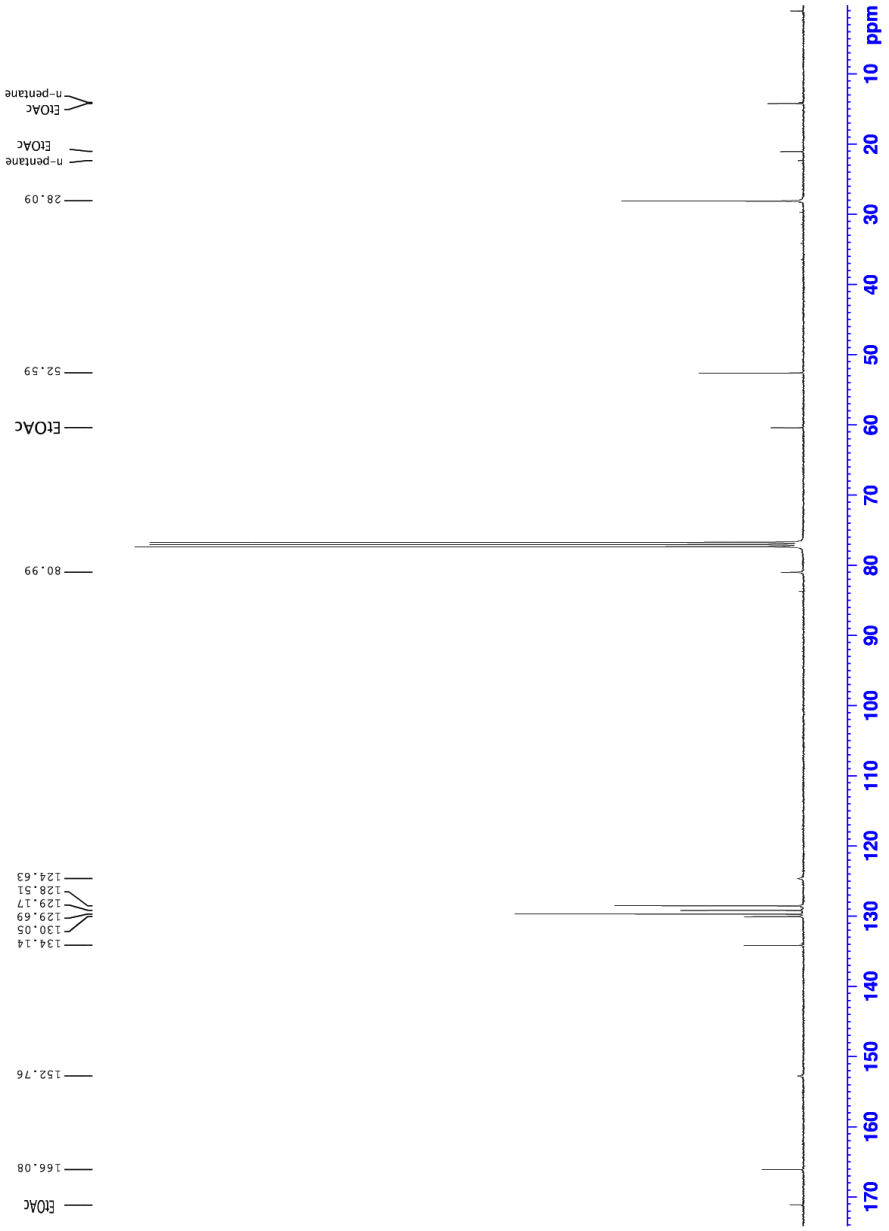

Figure E.2: The ^{13}C-NMR spectrum of **11**.

Appendix F

Diffraction patterns of MOFs

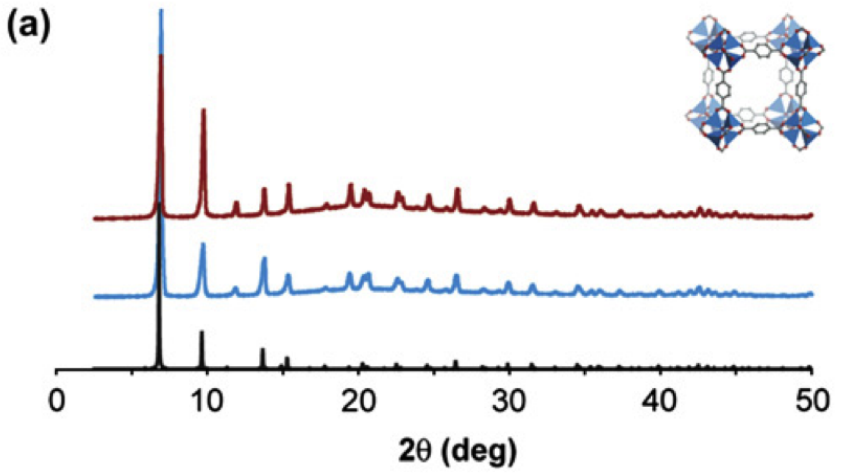

Figure F.1: The diffraction patterns of MOF-5 reported adopted from D. J. Tranchemontagne *et. al.*[17] The theoretical (black) diffract, from $Zn(NO_3)_2 \cdot 4\,H_2O$ (blue) and $Zn(OAc)_2 \cdot 2\,H_2O$ (red).

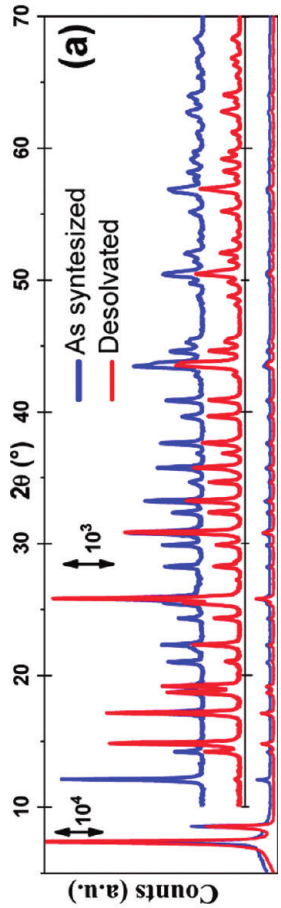

Figure F.2: The diffraction patterns for both the hydroxylated and dehydroxylated UIO-66 reported by Valenzano *et al.*.[4] Copyright 2011 ©American Chemical Society.